

Fully First-Principles Surface Spectroscopy with Machine LearningYair Litman,^{1,2} Jingtang Lan,^{3,4} Yuki Nagata,² and David M. Wilkins⁵

¹*Yusuf Hamied Department of Chemistry, University of Cambridge, Lensfield Road, Cambridge, CB2 1EW, UK*

²*Max Planck Institute for Polymer Research, Ackermannweg 10, 55128 Mainz, Germany^{a)}*

³*Department of Chemistry, New York University, New York, NY, 10003, USA*

⁴*Simons Center for Computational Physical Chemistry at New York University, New York, NY, 10003, USA*

⁵*Centre for Quantum Materials and Technology, School of Mathematics and Physics, Queen's University Belfast, Belfast BT7 1NN, Northern Ireland, United Kingdom^{b)}*

Our current understanding of the structure and dynamics of aqueous interfaces at the molecular level has grown substantially in the last few decades due to the continuous development of surface-specific spectroscopies, such as vibrational sum-frequency generation (VSFG). Similarly to what happens in other spectroscopies, to extract all of the information encoded in the VSFG spectra we must turn to atomistic simulations. The latter are conventionally based either on empirical force field models, which cannot describe bond breaking and formation or systems with a complex electronic structure, or on *ab initio* calculations which are difficult to statistically converge due to their computational cost. These limitations ultimately hamper our understanding of aqueous interfaces. In this work, we overcome these constraints by combining two machine learning techniques, namely high-dimensional neural network interatomic potentials and symmetry-adapted Gaussian process regression, to simulate the SFG spectra of the water/air interface with *ab initio* accuracy. Leveraging a data-driven local decomposition of atomic environments, we develop a simple scheme that allows us to obtain VSFG spectra in agreement with current experiments. Moreover, we identify the main sources of inaccuracy and establish a clear pathway towards the modelling of surface-sensitive spectroscopy of complex interfaces.

^{a)}Electronic mail: yl899@cam.ac.uk

^{b)}Electronic mail: d.wilkins@qub.ac.uk

Interfaces of aqueous solutions are ubiquitous in nature and play a crucial role in many important processes, such as (electro)catalytic applications¹, atmospheric aerosol–gas exchanges², and mineral dissolution³. In particular, the water/air interface has received enormous attention from the scientific community in the last few decades since it represents arguably the most simple and important interface with a hydrophobic surface and serves as a baseline from which more complex aqueous interfaces can be analyzed, interpreted and rationalized⁴. Water presents many interesting properties, such as anomalously high surface tension and a non-monotonic temperature dependence of its density with a maximum at 4°C⁵. These unique properties are attributed to its unusually strong hydrogen-bond (HB) networks. A fundamental understanding of the properties and reactivity of aqueous interfaces thus demands a molecular-level description that can capture the fine energetic balances governing the structural and dynamical characteristics of the HB networks^{6,7}.

Techniques that isolate the signal from the relatively few surface molecules at the surfaces from the enormous contribution due to the bulk are essential to study interfaces. Vibrational sum frequency generation (VSFG) belongs to a selected class of spectroscopic techniques with the capability of probing such interfaces with molecular-level and chemical sensitivity⁸. In VSFG experiments, IR and UV-visible pulses are spatially and temporally overlapped and a signal generated by the sample at the sum of the frequencies of the incoming radiations is measured. The signal is determined by the second order susceptibility of the sample, $\chi^{(2)}$. Since $\chi^{(2)}$ is zero in centrosymmetric (bulk) environments, it naturally provides information that emerges exclusively from interfacial molecules. The VSFG spectra of the O-H stretch mode at aqueous interfaces presents broad and featureless bands. Thus, experimental data alone is insufficient to unambiguously disentangle spectral components, and atomistic simulations are required for a microscopic understanding. Atomistic simulations have played an important role in settling the long-standing debate regarding the absence of a positive signal below 3200 cm⁻¹ for H₂O^{9,10}, in determining the dielectric function profile across the water interface¹¹, and in elucidating the pH-dependent structure at the fluorite/water interface¹².

The theoretical calculation of VSFG spectra is more challenging than that of more traditional spectroscopies such as linear IR and Raman, since relatively long simulation times, on the order of nanoseconds, are required to converge the statistics so that the signal in the bulk-like (centrosymmetric) regions vanishes^{13,14}. In this context, several approximations have been reported with different degrees of success when dealing with aqueous solutions. A first

group of studies is based on approximations of the potential energy surface (PES) by classically polarizable force fields¹³⁻¹⁶. Many important insights have been obtained with these approaches such as the determination of molecular orientation at interfaces¹⁷ or the proof that chiral VSFG exclusively probes the first hydration shell around biomolecules¹⁸. However, these calculations cannot describe the rearrangement of chemical bonds nor systems with complex electronic structure. A second important group is based on the combination of *ab initio* potentials at the density functional theory (DFT) level with approximations of the dipole and polarizability surfaces by simple models such as the surface-specific velocity-velocity correlation function formalism (ssVVCF)^{19,20} or frequency maps²¹. These approximations allow converged results to be obtained with relatively shorter simulations and deliver overall appropriate spectral shapes, including the absence of a positive signal below 3200 cm⁻¹ for H₂O^{9,19}. However, the oversimplified description of dipole and polarizability surfaces cannot distinguish between different polarization combinations, which is required for estimating the molecular orientation and studying the depth profile of molecules²². They are also unable to capture important spectral features originating from vibrational coupling²³⁻²⁶. Going beyond these approximations and obtaining a *fully ab initio* MD VSFG spectra of liquids is a long-sought goal in the SFG community, but due to prohibitively large computational expense, statistically converged simulations remain elusive²⁷.

The vibrational resonant component of the second order susceptibility, $\chi_{pqr}^{(2),R}$, in a electronically non-resonant condition, can be computed as¹³

$$\chi_{pqr}^{(2),R}(\omega_{\text{IR}}) = i \int_0^{\infty} dt e^{-i\omega_{\text{IR}}t} \langle \alpha_{pq}(t) P_r(0) \rangle, \quad (1)$$

where α_{pq} is the pq component of the polarizability tensor, ω_{IR} is frequency of the IR pulse, and P_r is the r component of the polarization vector. Hereafter, we refer to the resonant part exclusively so the R supraindex is omitted. The evaluation of Eq. 1 requires an accurate representation of three objects, namely, i) PES, ii) polarization surface (P -S) and iii) polarizability surface (α -S). Moreover, the light mass of hydrogen atoms, abundant in aqueous solutions, demands a quantum mechanical treatment of the molecular motions²⁸. In this work, the PES is evaluated using either DFT or Behler-Parrinello high-dimensional neural networks (HDNNP)²⁹, P -S and α -S are evaluated by a symmetry-adapted Gaussian process regression (SA-GPR) scheme that enables the prediction of tensorial quantities of arbitrary

order^{30,31}, and the time-evolution of the nuclei using classical molecular dynamics (MD), and centroid molecular dynamics (CMD)^{32,33} in its partially adiabatic approximation³⁴. The latter method is able to capture the most important nuclear quantum effects (NQE) in condensed phases, such as zero-point-energy and tunneling, and is suitable for spectroscopic simulations of aqueous solutions at room temperature^{28,35}.

The modelling of aqueous solution/air interfaces is normally performed by simulating the system under study in a slab geometry, in which the system extends infinitely along two dimensions and has finite size along the third dimension where it is sandwiched by regions of vacuum. This geometry gives two interfaces that will generate VSFG signals with opposite signs that cancel each other and lead to a vanishing signal. Thus, it is not possible to obtain any meaningful spectra if one uses P and α of the total slab in Eq. 1. As we will discuss below, our machine-learning (ML) approach offers an elegant and data-driven solution to this issue.

Training and Validation of ML models

SA-GPR predictions of a selected property, \mathbf{y} , can be expressed as a linear combination,

$$\mathbf{y}(\mathcal{X}) = \sum_I^{N_t} \sum_{i,j}^N w^I k^{(\lambda)}(\mathcal{X}_i, \mathcal{X}_j^I), \quad (2)$$

where $k^{(\lambda)}(\mathcal{X}_i, \mathcal{X}_j^I)$ is the kernel function that evaluates the similarity between the i^{th} atomic environment of the trial configuration, and the j^{th} atomic environment of the I^{th} reference configuration. N_t and N represent the number of training points and number of atomic environments, respectively, and $\{w^i\}$ are the weights determined during a training procedure³⁶. λ identifies an orthogonal subspace of dimension $2\lambda + 1$, according to SO(3) algebra³⁷, such that the modeling of P (α) requires the $\lambda = 1$ ($\lambda = 0, 2$) components. The training of the P -S and α -S was performed using DFT at the PBE and PBE0 level, and POLY2VS, a polarizable water force field developed by Tanimura and co-workers³⁸. The PBE and PBE0 data sets are obtained from first principles and constitutes the ultimate target of this work. The POLY2VS data set provides access to a molecular decomposition of the α and P quantities allowing us to critically assess the performance of the ML models. Moreover, we considered two types of data sets, one made up exclusively of bulk structures and a second one made of water clusters from monomers up to hexamers (see a more detailed description of the data

set and the training procedure in the Methods section below). We used the water HDNNP generated by Schran and co-workers using an active learning strategy³⁹. This model was trained on 814 reference data points including liquid, ice and slab structures at the revPBE0-D3 theory level, showing excellent agreement with the reference data. This level of theory is known to describe the structure and dynamics of liquid water accurately^{35,40}. To better evaluate the loss in accuracy in going from the *ab initio* PES to the HDNNP, we also considered the HDNNP published by some of the authors trained on slab structures at the revPBE-D3 theory level⁴¹.

In table I, we summarize the different models considered in this work. To enable comparisons between data sets, the error estimates are computed as the root mean square error (RMSE) percentage of the intrinsic deviation of the data set and expressed per water molecule. The SA-GPR models can accurately learn P and α with errors below a few percentages of the intrinsic variation in the training set. These values represent an error of 5.4×10^{-4} D/atom (7.6×10^{-4} D/atom) and 7.8×10^{-4} Å³/atom (1.1×10^{-3} Å³/atom) for $|P|$ and $\text{Tr}[\alpha]$, respectively, for the ML-POLY-B (ML-POLY-A) model. In the Supporting Information (SI), we report the correlation plots and learning curves of the ML models, together with a brief analysis of the training errors.

TABLE I. Root mean squared error (RMSE) for SA-GPR models of polarization per atom (in Debye) and polarizability per atom (in Å³). Numbers in brackets give the RMSE as a percentage of the intrinsic deviation in the training set.

Model Name	Configurations	Polarization (\mathbf{P})	Polarizability (α)
ML-POLY-A	Bulk Water	7.6×10^{-4} (1.7%)	2.7×10^{-3} (13%)
ML-POLY-B	Water clusters	5.4×10^{-4} (0.5%)	2.2×10^{-3} (3%)
ML-PBE-A	Bulk Water	1.0×10^{-3} (0.8%)	2.6×10^{-3} (13%)
ML-PBE0-A	Bulk Water	2.2×10^{-3} (0.8%)	–

ML aided simulation of VSFG spectra

As previously noted, $\chi^{(2)}$ for a slab geometry is zero due to a cancellation between the contributions of opposite interfaces. Assuming that the slab thickness is large enough to accommodate a bulk region in the middle and that a molecular decomposition of P is available,

it is standard practice to set to zero or flip the sign of the molecular dipoles below the centre of mass of the slab to avoid this cancellation^{19,20}. However, molecular dipoles are not observables and therefore they are arbitrary in nature. In *ab initio* calculations the molecular decomposition can be achieved by using maximally localized Wannier functions^{27,42}, which incurs the difficulty of requiring direct *ab initio* simulations⁴³. Here instead, we utilize an unbiased data-driven approach. Since we are using an atom-centred decomposition to represent the atomic environments, by rearranging the sums in Eq. 2, SA-GPR predictions can be expressed as a sum of molecular predictions as

$$\mathbf{y}(\mathcal{X}) = \sum_{\gamma} \mathbf{y}(\mathcal{X}_{\gamma}), \quad (3)$$

where γ represents the set of indices that corresponds to a given molecule. Thus, SA-GPR can be applied to the calculation of SA-GPR using Eq. 1 for slab geometries by applying the following modification to Eq. 3 for the P predictions

$$P(\mathcal{X}) = \sum_{\gamma} g(z_{\gamma})P(\mathcal{X}_{\gamma}), \quad (4)$$

where the surface plane is assumed to be parallel to the xy plane, z_{γ} is z coordinate of the γ molecule, and

$$g(z, z_1, z_2) = \text{sgn}(z) \times \begin{cases} 1 & |z - z_{\text{cm}}| \geq z_1 \\ \cos\left(\frac{(z_1 - |z - z_{\text{cm}}|)\pi}{2(z_1 - z_2)}\right) & z_1 \geq |z - z_{\text{cm}}| \geq z_2, \\ 0 & z_2 \geq |z - z_{\text{cm}}| \end{cases} \quad (5)$$

where z_{cm} is the z -coordinate of the slab center of mass, and z_1 and z_2 are two parameters that define the transition between the interfacial and bulk regions.

Global accuracy estimators, such as the RMSE and absolute error presented above, are useful indicators of the overall performance of ML models. However, when the learned quantities are used as a proxy for further calculations, as we do here for the calculation of $\chi^{(2),R}$, it is normally not possible to translate RMSE values directly into an objective accuracy measure of the final target. This is mainly because of the difficulty in performing a rigorous error propagation of the uncertainties in Eq. 1 but also due to the lack of a unique

set of descriptors to quantify how “good” a predicted spectrum is. In this work, we take what we consider to be the strictest validation test and in Fig. 1 compare the VSFG spectra of water obtained with our ML models against the corresponding reference POLY2VS spectra. We note that this can only be done because POLY2VS by construction has a molecular decomposition of P and α that enables the application of the filter function (Eq. 5). The $\text{Im}\chi^{(2)}$ spectrum of the water/air interface presents, irrespective of the polarization, a sharp positive peak centered at 3700 cm^{-1} and a broad band in the $3200\text{-}3500\text{ cm}^{-1}$ region with negative amplitude signal. The peak is due to the dangling (free) O-H group of the topmost interfacial water layer, and the band is associated with O-H groups of the interfacial water which form hydrogen-bonds with other water molecules. The sign of the amplitudes in the $\text{Im}\chi^{(2)}$ spectrum can be directly associated with the orientation of the water molecules. More specifically, positive (negative) amplitudes imply that the O-H group points towards the air (towards the bulk) phase. $\chi_{\text{pqr}}^{(2)}$ presents only 3 independent elements: $\chi_{zzz}^{(2)}$, $\chi_{zxx}^{(2)}$, and $\chi_{xxz}^{(2)}$. $\chi_{zxx}^{(2)} = \chi_{zyy}^{(2)} = \chi_{xzx}^{(2)} = \chi_{yzy}^{(2)}$, and $\chi_{xxz}^{(2)} = \chi_{yyz}^{(2)}$ due to the xy plane being isotropic and the symmetry of the polarizability tensor. The rest of the elements are exactly zero except for large chiral environments^{44,45}. In the case of the water/air interface, the non-zero $\text{Im}\chi^{(2)}$ tensor components differ essentially by the total intensity, the relative intensity of the free O-H and hydrogen-bonded O-H regions, and the presence or absence of a shoulder on the lower frequency side of the free O-H peak. The components have also a markedly different temperature dependence¹⁴.

We proceed with a systematic evaluation of the ML predictions of the VSFG spectra. First, we consider one PES given by the POLY2VS force-field and focus on the impact of different training sets used to create the SA-GPR models. Fig. 1a, Fig 1b, and Fig 1c show $\chi_{xxz}^{(2)}$, $\chi_{zzz}^{(2)}$, and $\chi_{zxx}^{(2)}$, respectively. The ML-POLY-A and ML-POLY-B models have similar accuracy in their predictions of $\chi_{xxz}^{(2)}$ and $\chi_{zzz}^{(2)}$ and provide a semi-quantitative agreement with the reference spectra. This is a rather surprising result since the ML-POLY-A model was trained in bulk water conformations and therefore has no information in the training set on interfacial water structures, whereas the ML-POLY-B model was trained on water cluster conformations, and had only limited information on fully solvated water molecules. The prediction of $\chi_{zxx}^{(2)}$ is considerably worse than the other two tensor components with ML-POLY-A performing only slightly better than ML-POLY-B for the free O-H peak. By performing cross-predictions using P/α from the ML model and α/P from the reference,

we identified the α predictions as the source of the observed inaccuracy (see Fig. S12 in the SI). This result highlights the limitation of using RMSE values and correlations plots as error estimators as all components of α show a comparable accuracy.

Electrostatic long range (LR) effects are known to play an important role at interfaces due to unbalanced interactions that can build up in the presence of a broken translation symmetry⁴⁶. The implications of using short-range models on structural properties of the water/air interface, such as orientations of water molecules or average density are well documented^{47,48}. ML models that include LR effects are also known to be more accurate^{46,49}. However, the possible impact on non-linear spectroscopic responses such as $\chi^{(2)}$ is less clear. To analyze this effect, we trained a long-distance equivariant (LODE) model based on the local value of an atom-density potentials⁴⁹. In Fig. 1c-d, we show the predictions using a combination of short range (SR) and LR, since the combined model normally delivers a superior accuracy than the individual ones. In particular, we considered different amounts of LR contributions in the range 50%-85%. The best combination across all the tensor components is obtained for a 25/75 SR/LR model, but the performance is very similar to that of SR models. These results unequivocally demonstrate that LR effects on the description of P and α do not have a huge impact on the $\chi^{(2)}$ spectra.

First principles simulation of VSFG spectra

Having established the suitability of the training set and the methodology, we now consider the spectral changes induced by different *ab initio* PES for fixed P and α surfaces. In Fig. 2, we present the computed VSFG spectra using ML-PBE-A and ML-POLY-A response surfaces and six different *ab initio* potential energy surfaces, namely PBE-D3, BLYP-D3, revPBE-D3, HSE06, B3LYP and revPBE0-D3. The trajectories were available from a previous work⁴⁰. Due to the limited length of the simulations, it was necessary to neglect intermolecular terms in Eq. 1 to obtain a reasonable converged spectrum (see more details in the SI). Thus, the width of the negative band is poorly described due to the absence of intermolecular couplings¹⁹. In all cases except for PBE-D3, the spectra do not show a positive signal below 2200 cm^{-1} in agreement with the latest measurements and simulations since 2015^{9,10}. In the case of D2O, the experimental free O-D amplitude is approximately 50% smaller than of the hydrogen bonded (HB) O-D band. For all the

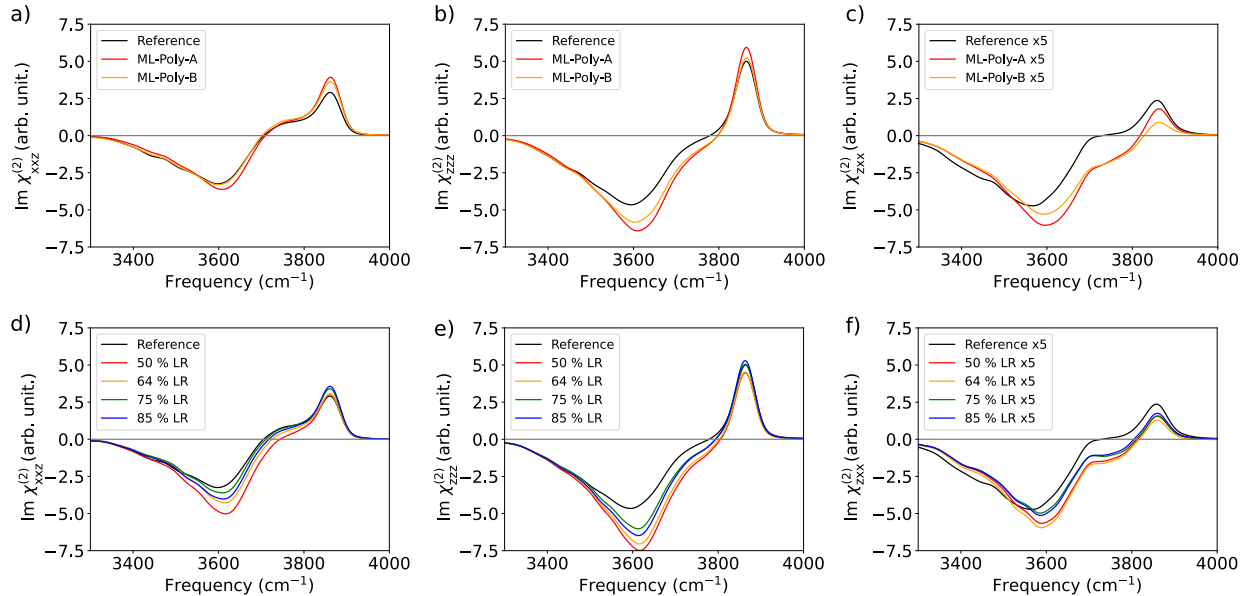


FIG. 1. a-c) Imaginary part of non-zero and independent $\chi^{(2)}$ components of the water/air interface using the POLY2VS model (reference) and ML-POLY-A and ML-POLY-B SA-GPR models. d-f) Same as a-c) but using ML-POLY-A augmented by different amounts of LR contributions. $\chi_{zzz}^{(2)}$ spectra are multiplied by a factor of 5 to ease visualization.

considered PESs, the ML-PBE-A model overestimates (underestimates) the intensity of free O-H peak (HB O-H band), while the ML-POLY-A model predicts relative intensities in better agreement with the experiments. The better performance of ML-POLY-A is a direct consequence of the fact that the reference POLY2VS dipole and polarizability surfaces were fitted to reproduce CCSD/aug-cc-pVQZ, rather than DFT, reference values. The calculations with GGA exchange correlation (XC) functionals (PBE-D3, BLYP and revPBE-D3) are artificially red-shifted in comparison to the results obtained with hybrid ones (HSE06, B3LYP and revPBE0-D3) in agreement with previous approximations based on the ssVVCF methodology⁴⁰, and results on bulk water^{35,50}. Inclusion of NQEs are known to induce a frequency red-shift when compared to the corresponding classical nuclei counterpart spectra^{28,51}. Thus, the frequency agreement between the revPBE-D3 PES and the experimental data is a fortuitous error compensation³⁵.

The intramolecular vibrational coupling of water molecules in which one O-H is a hydrogen-bond donor and the other one is free has a distinctive spectral feature associated with a shoulder on the free O-H peak. This shoulder has been assigned to the

asymmetric stretching mode of interfacial water molecules^{52,53} and contributions to this shoulder from water molecules forming two hydrogen bonds have been shown to be minor due to cancellation of inter- and intramolecular contributions¹⁴. PBE-D3, BLYP-D3, HSE06 and B3LYP spectra present a shoulder so separated from the free O-H peak that it can be regarded as a separate peak. On the contrary, this spectral feature is correctly displayed by the revPBE0-D3 and revPBE-D3 spectra. Moreover, the differences in performance for revPBE0-D3 and revPBE-D3 are relatively small and mainly impact the intensity of the free O-D peak and an overall frequency shift. These results show that even hybrid functionals considerably overestimate the H-bond strength, unlike in bulk water⁵⁴.

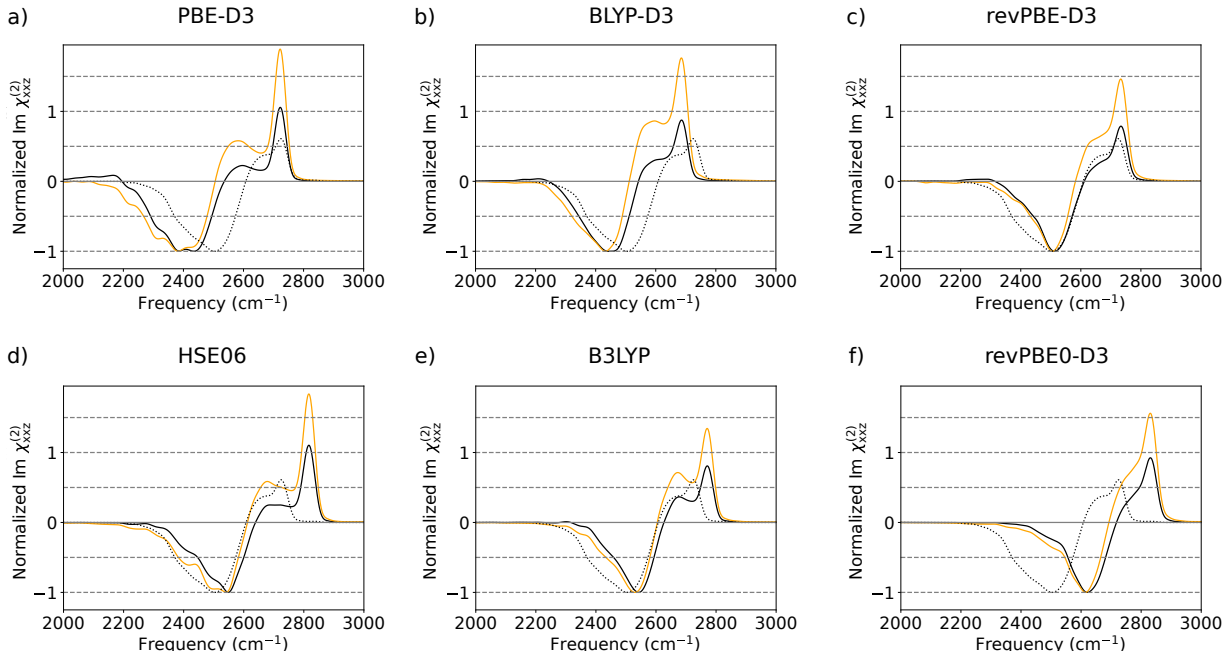


FIG. 2. Simulated SFG spectra, $(\chi_{xxz}^{(2)})$, of the water/air interface using trajectories obtained with *ab initio* PES and ML-PBE-A and ML-POLY-A are depicted by orange and black lines, respectively. Experimental spectra are corrected with Fresnel factors, assuming the Lorentz model for the interfacial dielectric constant is depicted in black dotted lines⁵⁵.

Finally, we show fully-ML predictions for the $\text{Im}\chi_{xxz}^{(2)}$ spectra for $\text{D}_2\text{O}/\text{air}$ at 300K in Fig. 3 ($\text{Re}\chi_{xxz}^{(2)}$ is reported in the SI). We focus on revPBE0-D3 and revPBE-D3 XC functionals since they show the best agreement with experiments. The solid red and dashed green curves show the predictions using the ML-POLY-A model and *ab initio* and HDNNP PES surfaces, respectively. The overall agreement between the spectra for each XC func-

tional is remarkable when considering the computational costs associated with each type of calculation. The revPBE0-D3 HDNNP result shows a free O-D peak with a more pronounced free O-D peak shoulder and a blue-shift of 33 cm^{-1} with respect to the *ab initio* one. Conversely, the revPBE0-D3 HDNNP spectra show a less pronounced free O-D peak shoulder and a red-shift of -14 cm^{-1} . Both HDNNP were trained without an explicit treatment of LR interactions which are known, as mentioned previously, to be responsible for the net orientation of the water molecules in the bulk region. We believe that these artefacts are responsible for the discrepancies with fully *ab initio* spectra. In particular, the spurious additional orientation of water molecules, which happens in opposite directions for revPBE-D3 and revPBE0-D3 HDNNPs, as shown in Fig. S14 in the SI, might be responsible for increasing and decreasing the splitting between free and HB O-D vibrations of water molecules at the topmost layer. For all tested cases, the theoretical predictions overestimate the intensity ratio between the free O-D and the hydrogen-bonded band. Such underestimation has been reported by Paesani and co-workers to be expected when neglecting induction effects arising from interactions between individual molecules⁵⁶. Since SA-GPR can capture local induction effects, the large discrepancy is attributed to the quality of the underlying reference data. Once more, the ML-POLY-A model outperforms the ML-PBE-A. For the revPBE0-D3 case, we also tested the the ML-PBE0-A, which uses PBE0 as reference data for P . While it represents an improvement with respect to revPBE-D3, particularly on the description of free O-D shoulder, it still underperforms the ML-POLY-A results.

So far we have analyzed simulations where the nuclei were assumed to behave classically, and the spectra have been rigidly red-shifted to account for the ignored NQEs. On the right panel of Fig. 3, we show the results obtained with CMD, which is a well-established method to simulate the vibrational spectra of condensed phase systems at room temperature including an approximated description of NQEs^{57,58}. CMD is based on the path integral formulation of quantum mechanics⁵⁹ and in this method the nuclei are evolved according to classical equations of motion on the so-called centroid potential of mean force. NQEs induce a small broadening of free O-D peak and HB-band and a red-shift of 81 cm^{-1} with respect to the corresponding classical nuclei simulations. However, the CMD spectrum is still 57 cm^{-1} blue-shifted with respect to the experimental result. We also obtained the VSFG spectra using the thermostated ring polymer molecular dynamics (TRPMD)⁶⁰ method which is known to deliver more accurate frequencies than CMD at 300 K since it does not suffer

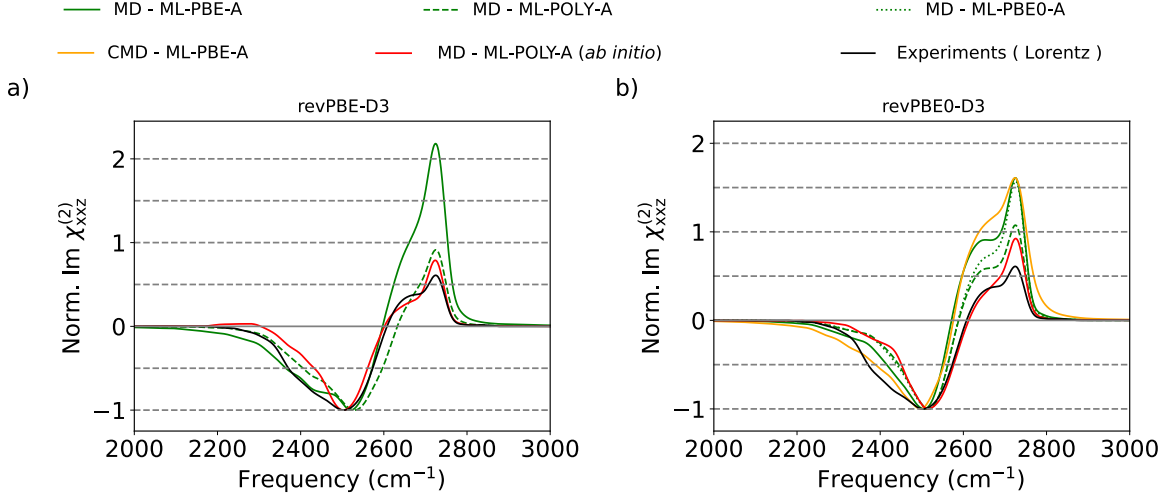


FIG. 3. Normalized $\chi_{xxz}^{(2)}$ spectra of the D_2O /air interface at 300K. Simulated spectra using revPBE-D3 (left) and revPBE0-D3 (right) XC functionals. Classical MD simulations using HDNNPs are presented by solid (ML-PBE-A), dashed (ML-POLY-A), and dotted (ML-PBE0-A) green lines. CMD simulations are depicted with solid orange lines while results based direct *ab initio* PES are depicted with red lines. Experimental spectra are depicted with solid black lines and horizontal gray lines have been added to guide the eye. Spectra have been rigidly shifted to match experimental spectra. The values of the frequency shifts for revPBE0-D3 (revPBE-D3) are: MD-HDNNP -138 cm^{-1} ($+4 \text{ cm}^{-1}$), MD-*ab initio* -105 cm^{-1} (-10 cm^{-1}), and CMD-HDNNP -57 cm^{-1} . Experimental spectra are corrected by the appropriate Fresnel factors, assuming the Lorentz model (black dotted lines) for the interfacial dielectric constant⁵⁵. To allow a visual comparative analysis, the spectra are normalized such that the HB O-D band has an intensity of unity.

from the curvature problem^{58,61–63} (see Fig. S16 in the SI). By comparing the CMD and TRPMD results, we deduce that the curvature problem is responsible for an additional 10 cm^{-1} red-shift. By accounting for the 33 cm^{-1} blue-shift induced by the lack of LR effects in the HDNNP discussed previously, we conclude that the error introduced by DFT in the revPBE0-D3 XC functional approximation is within the theoretical limit of quantum-statistic classical-dynamics methods which overestimate high-frequency modes by about 50 cm^{-1} ^{62,63}.

Discussion

The combination of two different types of ML algorithms, namely HDNNPs and SA-GPR, has allowed us to describe the water/air interface and its second-order response from first principles at an affordable computational cost. The training of the ML models were performed in a general fashion, without employing specific information of the system nature, such as physical constraints designed for water, mapping models for water²¹, or the use of a Δ ML procedure based on an available surrogate model⁶⁴. While at the moment force-fields tailored to describe water outperform the presented results^{11,14,55}, we stress that the procedure and strategy presented is directly applicable to any reference data set, to larger systems, and most importantly, to more complex interfaces.

We evaluated the impact of the different components that are involved in the calculation of the VSFG spectra. By comparing the performance of different XC, we found that the PES is better described by revPBE-D3 and revPBE0-D3 XC functionals. However, the VSFG spectrum is still 57 cm^{-1} blue-shifted when NQEs are properly taken into account. These results add to the existing evidence confirming that XC functionals constrained by exact functional conditions with suitable dispersion corrections, such as revPBE-D3 and revPBE0-D3, deliver excellent performance in the description of water³⁵.

Since the discrepancies between the theoretical and the experimental spectra are larger than the training error of the SA-GPR models, we attribute the largest source of error to the reference data used to describe the P and α surfaces. A further study using electronic structure methods beyond DFT to obtain more accurate P and α surfaces is urgently needed.

The modelling of the VSFG spectra was based on Eq. 1 which is derived in the electric dipole approximation⁶⁵. We believe that applying the current methodology to a more accurate reference data set would finally resolve existing controversies related to, for example, the relevance of quadrupole contributions in the water bending mode^{66,67}.

Two different methods were considered to describe the time evolution of the nuclei: MD and CMD. CMD is appropriate to describe the $\text{D}_2\text{O}/\text{air}$ interface and predicts a peak position in good agreement with experiments. However, the curvilinear motion of dangling O-H in H_2O shows an extremely broad feature^{56,68}, which calls for the use of other approaches which do not suffer from the curvature problem of CMD nor the broadening problem of TRPMD. The recent method proposed by Musil *et al.* seems a promising approach to

tackle these problems⁶⁹. We note, however, that none of these can describe accurately the Fermi resonance contributions^{55,62,70,71}.

We showed that the off-diagonal components of the α tensor for water are more difficult to learn due to their smaller magnitude when compared to the diagonal ones, which leads to a poorer description of certain $\chi^{(2)}$ matrix elements. Since spherical components mix together diagonal and off-diagonal elements, it is not possible to train the off-diagonal elements exclusively with current SA-GPR implementations. Future efforts will be directed in this direction, in the development of machine learning models to predict wannier centers⁷², and in the inclusion of explicit LR in the description of the PES.

In summary, the work presented here sets a new standard for atomistic simulation of non-linear spectroscopies of condensed phases. While we have focused on the second-order response which is related to VSFG spectroscopy, the approach presented here paves the way to *ab initio* simulations of 2D-VSFG, 2D-IR, 2D THz-Raman and 2D ThZ-IR-Vis spectroscopies⁷³⁻⁷⁵. We expect that applications of the same ideas would bring important atomistic insights into the properties of aqueous interfaces at metallic and biological surfaces⁴ in solution and under confinement⁷⁶.

MATERIALS AND METHODS

Molecular Dynamics Simulations

The water/air interface was modelled using a water slab made of 160 water molecules contained in a 16.63x16.63x44.14 Å³ simulation box. The simulations were carried out using the i-PI code⁷⁷ connected to the LAMMPS package^{78,79}. using the neural network potential reported in Ref.³⁹ and⁴¹. Unless specified otherwise, the results presented with classical nuclei MD were obtained as an average of 20 independent 100 ps trajectories in which the initial configurations were obtained by 100 ps thermalization runs at 300K using the stochastic velocity rescaling thermostat⁸⁰ with a time constant of 200 ps. The partially adiabatic CMD simulations were carried out using the same setup as reported elsewhere³⁵. In all cases, the configurations were saved every 4 fs in the production runs for a posterior calculation of P and α through the SA-GPR or POLY2VS³⁸ models. The *ab initio* trajectories were obtained from a previous work⁴⁰.

Symmetry-Adapted GPR Models

For each dataset, SA-GPR models were built for the polarization \mathbf{P} and the $\lambda = 0$ and $\lambda = 2$ spherical tensor components of the polarizability^{81,82}. We used the hyperparameters of Ref.⁸³, which were found to perform well for bulk water. The supplementary information includes scripts for the training procedure, in which the Cartesian tensor properties of the training set frames are converted to spherical tensors, the λ -SOAP descriptors of Ref.⁸¹ are calculated for each local environment in every training configuration and these are combined to give λ -SOAP kernels, which are used to train separate models for each spherical tensor component. The supplementary information includes a script that shows in detail how this process works. In each case, the full data set was split 80%:20% with the smaller set used to test the hyperparameters and ensure that the model was not overfit. The final model for each set was trained on the entire set. The SI also contains each of the models developed and a script that can be used to apply them. The mixed short-range/long-range models are built using kernels of the form,

$$\mathbf{K}^\lambda(\mathcal{X}, \mathcal{X}') = w_S \mathbf{K}_{\text{SR}}^\lambda(\mathcal{X}, \mathcal{X}') + w_L \mathbf{K}_{\text{LR}}^\lambda(\mathcal{X}, \mathcal{X}'), \quad (6)$$

where $\mathbf{K}^\lambda(\mathcal{X}, \mathcal{X}')$ is the total spherical tensor kernel of order λ between two local environments \mathcal{X} and \mathcal{X}' , $\mathbf{K}_{\text{SR}}^\lambda$ is the (short-ranged) λ -SOAP kernel⁸¹, $\mathbf{K}_{\text{LR}}^\lambda$ the (long-ranged) λ -LODE kernel⁴⁹ and $w_S + w_L = 1$

For the ML-PBE-A model, we used the bulk water data of Ref.⁸¹, comprising 1000 frames of 32 molecules, with polarizations and polarizabilities computed using the PBE functional and ultrasoft pseudopotentials. For these 1000 frames, the polarizations were recomputed at the PBE0 level to produce the ML-PBE0-A set. These configurations were also used for the ML-POLY-A set, with both the polarization and the polarizability recomputed with the POLY2VS model. The ML-POLY-B models were produced using a set of water clusters: water n -mer configurations (with $n = 1, \dots, 6$) were taken from the training set used in Ref.⁸⁴: 10,000 clusters were used for each value of n , with the POLY2VS model used to calculate the dipole moment $\boldsymbol{\mu}$ and $\boldsymbol{\alpha}$. The predictions of ML-POLY-B give atom-centred dipole moments, which can be summed up to give a prediction of the total polarization of a frame.

The accuracy of SA-GPR models for the polarizability is given by the root mean squared

error (RMSE),

$$\text{RMSE}_\alpha = \sqrt{\frac{1}{N} \sum_{i=1}^N \|\alpha_{\text{calc},i} - \alpha_{\text{pred},i}\|_2^2}, \quad (7)$$

where $\|\cdots\|_2$ is the Frobenius norm, N the number of members of the training set, $\alpha_{\text{calc},i}$ the calculated polarizability for the i^{th} testing point and $\alpha_{\text{pred},i}$ its predicted polarizability. For the polarization we use,

$$\text{RMSE}_P = \sqrt{\frac{1}{N} \sum_{i=1}^N \||\mathbf{P}|_{\text{calc},i} - |\mathbf{P}|_{\text{pred},i}\|_2^2}, \quad (8)$$

with $\|\mathbf{P}\|_{\text{calc},i}$ the magnitude of the calculated polarization of testing point i and $\|\mathbf{P}\|_{\text{pred},i}$ its predicted value.

ACKNOWLEDGMENTS

Y.L. has been partly funded by the Deutsche Forschungsgemeinschaft (DFG, German Research Foundation) project number 467724959. D.M.W. thanks Queen’s University Belfast for startup funding. J.L. thanks Simons Foundation Postdoctoral Fellowship. We thank Dr. Venkat Kapil for the useful discussion. We acknowledge the computing resources from the Swiss National Supercomputing Centre (CSCS) under project ID S1112, S1113.

REFERENCES

- ¹O. M. Magnussen and A. Groß, “Toward an atomic-scale understanding of electrochemical interface structure and dynamics,” *Journal of the American Chemical Society* **141**, 4777–4790 (2019).
- ²A. M. Jubb, W. Hua, and H. C. Allen, “Environmental chemistry at vapor/water interfaces: Insights from vibrational sum frequency generation spectroscopy,” *Annual Review of Physical Chemistry* **63**, 107–130 (2012).
- ³J. Schott, O. S. Pokrovsky, and E. H. Oelkers, “The Link Between Mineral Dissolution/Precipitation Kinetics and Solution Chemistry,” *Reviews in Mineralogy and Geochemistry* **70**, 207–258 (2009), https://pubs.geoscienceworld.org/msa/rimg/article-pdf/70/1/207/2950086/207_06_Schott_etal.pdf.

- ⁴G. Gonella, E. H. G. Backus, Y. Nagata, D. J. Bonthuis, P. Loche, A. Schlaich, R. R. Netz, A. Kühnle, I. T. McCrum, M. T. M. Koper, M. Wolf, B. Winter, G. Meijer, R. K. Campen, and M. Bonn, “Water at charged interfaces,” *Nature Reviews Chemistry* **5**, 466–485 (2021).
- ⁵L. G. M. Pettersson, R. H. Henchman, and A. Nilsson, “Water—the most anomalous liquid,” *Chemical Reviews* **116**, 7459–7462 (2016).
- ⁶C. J. Fecko, J. D. Eaves, J. J. Loparo, A. Tokmakoff, and P. L. Geissler, “Ultrafast hydrogen-bond dynamics in the infrared spectroscopy of water,” *Science* **301**, 1698–1702 (2003), <https://www.science.org/doi/pdf/10.1126/science.1087251>.
- ⁷O. Björneholm, M. H. Hansen, A. Hodgson, L.-M. Liu, D. T. Limmer, A. Michaelides, P. Pedevilla, J. Rossmeisl, H. Shen, G. Tocci, E. Tyrode, M.-M. Walz, J. Werner, and H. Bluhm, “Water at interfaces,” *Chemical Reviews* **116**, 7698–7726 (2016).
- ⁸Y. R. Shen, “Surface properties probed by second-harmonic and sum-frequency generation,” *Nature* **337**, 519–525 (1989).
- ⁹S. Nihonyanagi, R. Kusaka, K.-i. Inoue, A. Adhikari, S. Yamaguchi, and T. Tahara, “Accurate determination of complex $\chi(2)$ spectrum of the air/water interface,” *J. Chem. Phys.* **143**, 124707 (2015).
- ¹⁰F. Tang, T. Ohto, S. Sun, J. R. Rouxel, S. Imoto, E. H. G. Backus, S. Mukamel, M. Bonn, and Y. Nagata, “Molecular structure and modeling of water–air and ice–air interfaces monitored by sum-frequency generation,” *Chem. Rev.* **120**, 3633–3667 (2020).
- ¹¹K.-Y. Chiang, T. Seki, C.-C. Yu, T. Ohto, J. Hunger, M. Bonn, and Y. Nagata, “The dielectric function profile across the water interface through surface-specific vibrational spectroscopy and simulations,” *Proceedings of the National Academy of Sciences* **119**, e2204156119 (2022), <https://www.pnas.org/doi/pdf/10.1073/pnas.2204156119>.
- ¹²R. Khatib, E. H. G. Backus, M. Bonn, M.-J. Perez-Haro, M.-P. Gageot, and M. Sulpizi, “Water orientation and hydrogen-bond structure at the fluorite/water interface,” *Scientific Reports* **6**, 24287 (2016).
- ¹³A. Morita and J. T. Hynes, “A theoretical analysis of the sum frequency generation spectrum of the water surface. ii. time-dependent approach,” *J. Phys. Chem. B* **106**, 673–685 (2002).
- ¹⁴D. R. Moberg, S. C. Straight, and F. Paesani, “Temperature dependence of the air/water interface revealed by polarization sensitive sum-frequency generation spectroscopy,” *J.*

- Phys. Chem. B **122**, 4356–4365 (2018).
- ¹⁵Y. Nagata, C.-S. Hsieh, T. Hasegawa, J. Voll, E. H. G. Backus, and M. Bonn, “Water bending mode at the water–vapor interface probed by sum-frequency generation spectroscopy: A combined molecular dynamics simulation and experimental study,” *J. Phys. Chem. Lett.* **4**, 1872–1877 (2013).
- ¹⁶R. Khatib, T. Hasegawa, M. Sulpizi, E. H. G. Backus, M. Bonn, and Y. Nagata, “Molecular dynamics simulations of sfg librational modes spectra of water at the water–air interface,” *J. Phys. Chem. C* **120**, 18665–18673 (2016).
- ¹⁷C.-C. Yu, T. Seki, Y. Wang, M. Bonn, and Y. Nagata, “Polarization-dependent sum-frequency generation spectroscopy for ångstrom-scale depth profiling of molecules at interfaces,” *Phys. Rev. Lett.* **128**, 226001 (2022).
- ¹⁸D. Konstantinovsky, E. A. Perets, T. Santiago, L. Velarde, S. Hammes-Schiffer, and E. C. Y. Yan, “Detecting the first hydration shell structure around biomolecules at interfaces,” *ACS Central Science* **8**, 1404–1414 (2022).
- ¹⁹T. Ohto, K. Usui, T. Hasegawa, M. Bonn, and Y. Nagata, “Toward ab initio molecular dynamics modeling for sum-frequency generation spectra; an efficient algorithm based on surface-specific velocity-velocity correlation function,” *J. Chem. Phys.* **143**, 124702 (2015).
- ²⁰R. Khatib and M. Sulpizi, “Sum frequency generation spectra from velocity–velocity correlation functions,” *J. Phys. Chem. Lett.* **8**, 1310–1314 (2017).
- ²¹Y. Ni and J. L. Skinner, “Ir and sfg vibrational spectroscopy of the water bend in the bulk liquid and at the liquid-vapor interface, respectively,” *J. Chem. Phys.* **143**, 014502 (2015).
- ²²C.-C. Yu, T. Seki, K.-Y. Chiang, F. Tang, S. Sun, M. Bonn, and Y. Nagata, “Polarization-dependent heterodyne-detected sum-frequency generation spectroscopy as a tool to explore surface molecular orientation and Ångström-scale depth profiling,” *J. Phys. Chem. B* **126**, 6113–6124 (2022).
- ²³C.-S. Tian and Y. R. Shen, “Isotopic dilution study of the water/vapor interface by phase-sensitive sum-frequency vibrational spectroscopy,” *J. Am. Chem. Soc.* **131**, 2790–2791 (2009).
- ²⁴S. Nihonyanagi, T. Ishiyama, T.-k. Lee, S. Yamaguchi, M. Bonn, A. Morita, and T. Tahara, “Unified molecular view of the air/water interface based on experimental and theoretical x(2) spectra of an isotopically diluted water surface,” *J. Am. Chem. Soc.* **133**, 16875–16880 (2011).

- ²⁵S. Yamaguchi, T. Takayama, Y. Goto, T. Otsu, and T. Yagasaki, “Experimental and theoretical heterodyne-detected sum frequency generation spectroscopy of isotopically pure and diluted water surfaces,” *J. Phys. Chem. Lett.* **13**, 9649–9653 (2022).
- ²⁶K.-Y. Chiang, X. Yu, C.-C. Yu, T. Seki, S. Sun, M. Bonn, and Y. Nagata, “Bulk-like vibrational coupling of surface water revealed by sum-frequency generation spectroscopy,” *ChemRxiv* (2022), 10.26434/chemrxiv-2022-xnwbq.
- ²⁷D. Ojha and T. D. Kühne, ““on-the-fly” calculation of the vibrational sum-frequency generation spectrum at the air-water interface,” *Molecules* **25** (2020), 10.3390/molecules25173939.
- ²⁸T. E. Markland and M. Ceriotti, “Nuclear quantum effects enter the mainstream,” *Nature Reviews Chemistry* **2**, 0109 (2018).
- ²⁹J. Behler and M. Parrinello, “Generalized neural-network representation of high-dimensional potential-energy surfaces,” *Phys. Rev. Lett.* **98**, 146401 (2007).
- ³⁰A. Grisafi, D. M. Wilkins, G. Csányi, and M. Ceriotti, “Symmetry-adapted machine learning for tensorial properties of atomistic systems,” *Phys. Rev. Lett.* **120**, 036002 (2018).
- ³¹V. L. Deringer, A. P. Bartók, N. Bernstein, D. M. Wilkins, M. Ceriotti, and G. Csányi, “Gaussian process regression for materials and molecules,” *Chem. Rev.* **121**, 10073 (2021).
- ³²S. Jang and G. A. Voth, “A derivation of centroid molecular dynamics and other approximate time evolution methods for path integral centroid variables,” *J. Chem. Phys.* **111**, 2371–2384 (1999).
- ³³J. Cao and G. A. Voth, “The formulation of quantum statistical mechanics based on the feynman path centroid density. ii. dynamical properties,” *J. Chem. Phys.* **100**, 5106–5117 (1994).
- ³⁴T. D. Hone, P. J. Rossky, and G. A. Voth, “A comparative study of imaginary time path integral based methods for quantum dynamics,” *J. Chem. Phys.* **124**, 154103 (2006).
- ³⁵O. Marsalek and T. E. Markland, “Quantum dynamics and spectroscopy of ab initio liquid water: The interplay of nuclear and electronic quantum effects,” *J. Phys. Chem. Lett.* **8**, 1545–1551 (2017).
- ³⁶T. Hastie, R. Tibshirani, and J. Friedman, *The Elements of Statistical Learning, 2nd ed.* (Springer, New York, 2009).
- ³⁷U. Weinert, “Spherical tensor representation,” *Archive for Rational Mechanics and Analysis* **74**, 165–196 (1980).

- ³⁸T. Hasegawa and Y. Tanimura, “A polarizable water model for intramolecular and intermolecular vibrational spectroscopies,” *J. Phys. Chem. B* **115**, 5545–5553 (2011).
- ³⁹C. Schran, K. Brezina, and O. Marsalek, “Committee neural network potentials control generalization errors and enable active learning,” *J. Chem. Phys.* **153**, 104105 (2020).
- ⁴⁰T. Ohto, M. Dodia, J. Xu, S. Imoto, F. Tang, F. Zysk, T. D. Kühne, Y. Shigeta, M. Bonn, X. Wu, and Y. Nagata, “Accessing the accuracy of density functional theory through structure and dynamics of the water–air interface,” *J. Phys. Chem. Lett.* **10**, 4914–4919 (2019).
- ⁴¹Y. Litman, K.-Y. Chiang, T. Seki, Y. Nagata, and M. Bonn, “The surface of electrolyte solutions is stratified,” *arXiv*, 2210.01527 (2022).
- ⁴²Q. Wan and G. Galli, “First-principles framework to compute sum-frequency generation vibrational spectra of semiconductors and insulators,” *Phys. Rev. Lett.* **115**, 246404 (2015).
- ⁴³D. Marx and J. Hutter, *Ab Initio Molecular Dynamics: Basic Theory and Advanced Methods* (Cambridge University Press, 2009).
- ⁴⁴J. Wang, X. Chen, M. L. Clarke, and Z. Chen, “Detection of chiral sum frequency generation vibrational spectra of proteins and peptides at interfaces in situ,” *Proceedings of the National Academy of Sciences* **102**, 4978–4983 (2005).
- ⁴⁵E. A. Perets, K. B. Olesen, and E. C. Y. Yan, “Chiral sum frequency generation spectroscopy detects double-helix dna at interfaces,” *Langmuir* **38**, 5765–5778 (2022).
- ⁴⁶S. P. Niblett, M. Galib, and D. T. Limmer, “Learning intermolecular forces at liquid–vapor interfaces,” *The Journal of Chemical Physics* **155**, 164101 (2021), <https://doi.org/10.1063/5.0067565>.
- ⁴⁷S. Yue, M. C. Muniz, M. F. Calegari Andrade, L. Zhang, R. Car, and A. Z. Panagiotopoulos, “When do short-range atomistic machine-learning models fall short?” *J. Chem. Phys.* **154**, 034111 (2021).
- ⁴⁸A. Gao and R. C. Remsing, “Self-consistent determination of long-range electrostatics in neural network potentials,” *Nature Communications* **13**, 1572 (2022).
- ⁴⁹A. Grisafi and M. Ceriotti, “Incorporating long-range physics in atomic-scale machine learning,” *J. Chem. Phys.* **151**, 204105 (2019).
- ⁵⁰M. J. Gillan, D. Alfè, and A. Michaelides, “Perspective: How good is dft for water?” *J. Chem. Phys.* **144**, 130901 (2016).
- ⁵¹R. L. Benson, G. Trenins, and S. C. Althorpe, “Which quantum statistics–classical dy-

- namics method is best for water?” *Faraday Discuss.* **221**, 350–366 (2020).
- ⁵²J. Schaefer, E. H. G. Backus, Y. Nagata, and M. Bonn, “Both inter- and intramolecular coupling of o–h groups determine the vibrational response of the water/air interface,” *J. Phys. Chem. Lett.* **7**, 4591–4595 (2016).
- ⁵³I. V. Stiopkin, C. Weeraman, P. A. Pieniazek, F. Y. Shalhout, J. L. Skinner, and A. V. Benderskii, “Hydrogen bonding at the water surface revealed by isotopic dilution spectroscopy,” *Nature* **474**, 192–195 (2011).
- ⁵⁴M. Guidon, F. Schiffmann, J. Hutter, and J. VandeVondele, “Ab initio molecular dynamics using hybrid density functionals,” *J. Chem. Phys.* **128**, 214104 (2008).
- ⁵⁵X. Yu, K.-Y. Chiang, C.-C. Yu, M. Bonn, and Y. Nagata, “On the fresnel factor correction of sum-frequency generation spectra of interfacial water,” *J. Chem. Phys.* **158**, 044701 (2023).
- ⁵⁶G. R. Medders and F. Paesani, “Dissecting the molecular structure of the air/water interface from quantum simulations of the sum-frequency generation spectrum,” *J. Am. Chem. Soc.* **138**, 3912–3919 (2016).
- ⁵⁷S. Habershon, G. S. Fanourgakis, and D. E. Manolopoulos, “Comparison of path integral molecular dynamics methods for the infrared absorption spectrum of liquid water,” *J. Chem. Phys.* **129**, 074501 (2008).
- ⁵⁸M. Rossi, H. Liu, F. Paesani, J. Bowman, and M. Ceriotti, “Communication: On the consistency of approximate quantum dynamics simulation methods for vibrational spectra in the condensed phase,” *J. Chem. Phys.* **141**, 181101 (2014).
- ⁵⁹R. P. Feynman and A. R. Hibbs, *Quantum Mechanics and Path Integrals* (McGraw-Hill, 1965).
- ⁶⁰M. Rossi, M. Ceriotti, and D. E. Manolopoulos, “How to remove the spurious resonances from ring polymer molecular dynamics,” *J. Chem. Phys.* **140**, 234116 (2014).
- ⁶¹S. D. Ivanov, A. Witt, M. Shiga, and D. Marx, “Communications: On artificial frequency shifts in infrared spectra obtained from centroid molecular dynamics: Quantum liquid water,” *J. Chem. Phys.* **132**, 031101 (2010).
- ⁶²S. C. Althorpe, “Path-integral approximations to quantum dynamics,” *Eur. Phys. J. B* **94**, 155 (2021).
- ⁶³G. Trenins, M. J. Willatt, and S. C. Althorpe, “Path-integral dynamics of water using curvilinear centroids,” *J. Chem. Phys.* **151**, 054109 (2019).

- ⁶⁴C. Qu, Q. Yu, R. Conte, P. L. Houston, A. Nandi, and J. M. Bowman, “A delta-machine learning approach for force fields, illustrated by a ccscd(t) 4-body correction to the mb-pol water potential,” *Digital Discovery* **1**, 658–664 (2022).
- ⁶⁵A. Morita, *Theory of Sum Frequency Generation Spectroscopy* (Springer Nature Singapore, Singapore, 2018) pp. 151–200.
- ⁶⁶A. Kundu, S. Tanaka, T. Ishiyama, M. Ahmed, K.-i. Inoue, S. Nihonyanagi, H. Sawai, S. Yamaguchi, A. Morita, and T. Tahara, “Bend vibration of surface water investigated by heterodyne-detected sum frequency generation and theoretical study: Dominant role of quadrupole,” *J. Phys. Chem. Lett.* **7**, 2597–2601 (2016).
- ⁶⁷T. Seki, K.-Y. Chiang, C.-C. Yu, X. Yu, M. Okuno, J. Hunger, Y. Nagata, and M. Bonn, “The bending mode of water: A powerful probe for hydrogen bond structure of aqueous systems,” *J. Phys. Chem. Lett.* **11**, 8459–8469 (2020).
- ⁶⁸N. K. Kaliannan, A. H. Aristizabal, H. Wiebeler, F. Zysk, T. Ohto, Y. Nagata, and T. D. Kühne, “Impact of intermolecular vibrational coupling effects on the sum-frequency generation spectra of the water/air interface,” *Molecular Physics* **118**, 1620358 (2020).
- ⁶⁹F. Musil, I. Zaporozhets, F. Noé, C. Clementi, and V. Kapil, “Quantum dynamics using path integral coarse-graining,” *J. Chem. Phys.* **157**, 181102 (2022).
- ⁷⁰R. L. Benson and S. C. Althorpe, “On the “matsubara heating” of overtone intensities and fermi splittings,” *J. Chem. Phys.* **155**, 104107 (2021).
- ⁷¹T. Plé, S. Huppert, F. Finocchi, P. Depondt, and S. Bonella, “Anharmonic spectral features via trajectory-based quantum dynamics: A perturbative analysis of the interplay between dynamics and sampling,” *J. Chem. Phys.* **155**, 104108 (2021).
- ⁷²L. Zhang, M. Chen, X. Wu, H. Wang, W. E, and R. Car, “Deep neural network for the dielectric response of insulators,” *Phys. Rev. B* **102**, 041121 (2020).
- ⁷³F. Perakis, L. De Marco, A. Shalit, F. Tang, Z. R. Kann, T. D. Kühne, R. Torre, M. Bonn, and Y. Nagata, “Vibrational spectroscopy and dynamics of water,” *Chemical Reviews* **116**, 7590–7607 (2016).
- ⁷⁴J. Savolainen, S. Ahmed, and P. Hamm, “Two-dimensional raman-terahertz spectroscopy of water,” *Proceedings of the National Academy of Sciences* **110**, 20402–20407 (2013).
- ⁷⁵M. Grechko, T. Hasegawa, F. D’Angelo, H. Ito, D. Turchinovich, Y. Nagata, and M. Bonn, “Coupling between intra- and intermolecular motions in liquid water revealed by two-dimensional terahertz-infrared-visible spectroscopy,” *Nature Communications* **9**, 885

- (2018).
- ⁷⁶V. Kapil, C. Schran, A. Zen, J. Chen, C. J. Pickard, and A. Michaelides, “The first-principles phase diagram of monolayer nanoconfined water,” *Nature* **609**, 512–516 (2022).
- ⁷⁷V. Kapil, M. Rossi, O. Marsalek, R. Petraglia, Y. Litman, T. Spura, B. Cheng, A. Cuzzocrea, R. H. Meißner, D. M. Wilkins, B. A. Helfrecht, P. Juda, S. P. Bienvenue, W. Fang, J. Kessler, I. Poltavsky, S. Vandenbrande, J. Wieme, C. Corminboeuf, T. D. Kühne, D. E. Manolopoulos, T. E. Markland, J. O. Richardson, A. Tkatchenko, G. A. Tribello, V. V. Speybroeck, and M. Ceriotti, “i-pi 2.0: A universal force engine for advanced molecular simulations,” *Comp. Phys. Commun.* **236**, 214–223 (2019).
- ⁷⁸A. P. Thompson, H. M. Aktulga, R. Berger, D. S. Bolintineanu, W. M. Brown, P. S. Crozier, P. J. i. t. Veld, A. Kohlmeyer, S. G. Moore, T. D. Nguyen, R. Shan, M. J. Stevens, J. Tranchida, C. Trott, and S. J. Plimpton, “LAMMPS - a flexible simulation tool for particle-based materials modeling at the atomic, meso, and continuum scales,” *Computer Physics Communications* **271**, 108171 (2022).
- ⁷⁹A. Singraber, J. Behler, and C. Dellago, “Library-based lammmps implementation of high-dimensional neural network potentials,” *Journal of Chemical Theory and Computation* **15**, 1827–1840 (2019).
- ⁸⁰G. Bussi, D. Donadio, and M. Parrinello, “Canonical sampling through velocity rescaling,” *J. Chem. Phys.* **126**, 014101 (2007).
- ⁸¹A. Grisafi, D. M. Wilkins, G. Csányi, and M. Ceriotti, “Symmetry-Adapted Machine Learning for Tensorial Properties of Atomistic Systems,” *Physical Review Letters* **120**, 036002 (2018).
- ⁸²D. M. Wilkins, A. Grisafi, Y. Yang, K.-U. Lao, R. A. DiStasio, and M. Ceriotti, “Accurate Molecular Polarizabilities with Coupled Cluster Theory and Machine Learning,” *Proc. Natl. Acad. Sci.* **116**, 3401 (2019), [arXiv:/arxiv.org/abs/1809.05349](https://arxiv.org/abs/1809.05349) [https:].
- ⁸³V. Kapil, D. M. Wilkins, J. Lan, and M. Ceriotti, “Inexpensive Modelling of Quantum Dynamics using Path Integral Generalized Langevin Equation Thermostats,” *J. Chem. Phys.* **152**, 124194 (2020), [arXiv:/arxiv.org/abs/1912.03189](https://arxiv.org/abs/1912.03189) [https:].
- ⁸⁴K. Inoue, Y. Litman, D. M. Wilkins, Y. Nagata, and M. Okuno, “Is unified understanding of vibrational coupling of water possible? hyper-raman measurement and machine learning spectra,” *J. Phys. Chem. Lett.* **14**, 3063 (2023).

Fully First-Principles Surface Spectroscopy with Machine LearningY. Litman,^{1,2} Jingtang Lan,^{3,4} Yuki Nagata,² and David M. Wilkins⁵

¹*Yusuf Hamied Department of Chemistry, University of Cambridge, Lensfield Road, Cambridge, CB2 1EW, UK*

²*Max Planck Institute for Polymer Research, Ackermannweg 10, 55128 Mainz, Germany*

³*Department of Chemistry, New York University, New York, NY, 10003, USA*

⁴*Simons Center for Computational Physical Chemistry at New York University, New York, NY, 10003, USA*

⁵*Centre for Quantum Materials and Technology, School of Mathematics and Physics, Queen's University Belfast, Belfast BT7 1NN, Northern Ireland, United Kingdom*

METHODS

More details on the calculation of the VSFG spectra

By introducing Eq. 3 and 4 into Eq. 1, we obtain

$$\chi_{pqr}^{(2),R}(\omega_{\text{IR}}) = i \int_0^\infty dt e^{-i\omega_{\text{IR}}t} \sum_{\gamma_1, \gamma_2} \langle g(z_{\gamma_2}, z_1, z_2) \alpha_{pq}(\mathcal{X}_{\gamma_1}, t) P_r(\mathcal{X}_{\gamma_2}, 0) \rangle, \quad (1)$$

where $\alpha_{pq}(\mathcal{X}_{\gamma_1}, t)$ is the polarizability of the molecule γ_1 at time t and $P_r(\mathcal{X}_{\gamma_2}, 0)$ is the molecular dipole of the molecule γ_2 at time 0. The surface normal is assumed to be parallel to the z -axis and z_{γ_2} corresponds to z coordinate of the γ_2 water molecule. The results obtained from the *ab initio* trajectories (Fig. 3 of the main text) were calculated by considering only the terms $\gamma_1 = \gamma_2$ in the sum of Eq. 1. This approximation was necessary due to the limited length of the trajectories. For all the other results, the sum was evaluated for all pairs of water molecules separated by less than 4 Å. This cutoff value provides a converged spectra, see for example¹. Unless specified, we use $z_1 = 4$ Å and $z_2 = 2$ Å as reported in Ref.², and before the calculation of the Fourier transform the correlation function was convoluted with a Hahn window such that it decays to zero after 1.0 ps. Experimental data was processed consistently.

Hybrid DFT Calculations

The hybrid PBE0 calculations were performed using the CP2K program³. Molecular orbitals of the valence electrons were expanded in the TZV2P basis sets⁴, while atomic core electrons were described through Goedecker-Teter-Hutter (GTH) pseudopotentials corresponding to the PBE functional^{5,6}. Exact exchange integrals were calculated within the auxiliary density matrix method (ADMM) approximation⁷. In addition, the truncated Coulomb operator⁸ has been applied for the exchange calculations with the cutoff radius approximately equal to half the length of the smallest edge of the simulation cell, together with the Schwarz integral screening with the threshold of 10^{-10} a. u. The cutoff for the auxiliary plane waves was 800 Ry.

The total electric dipole moment μ is evaluated using the Berry phase scheme^{9,10}. With a side length L and considering only the Γ point in the Brillouin zone, each component of

the electric-dipole moment is then

$$\mu = \frac{e}{2\pi} \text{Im} \ln \det \mathbf{S}, \quad (2)$$

where the matrix \mathbf{S} is defined using the Kohn-Sam orbitals ϕ_n , and

$$S_{n,m}(x) = \int_L \phi_n^*(x) \exp \left[-i \frac{2\pi}{L} x \right] \phi_m(x) dx. \quad (3)$$

The polarizability α is calculated using the finite difference method, where a periodic electric field is applied in a given direction.

$$\alpha = \frac{d\mu}{dE}. \quad (4)$$

TRAINING OF SA-GPR MODELS

The learning curves for polarization (P) and polarizability (α) for ML-POLY-A and ML-POLY-B models are presented in Fig. 1 and 2, respectively. The learning curves for ML-PBE-A can be found elsewhere¹¹ and P learning curve for ML-PBE0-A is presented in Fig. 3. In Fig. 4 (6) and 5 (7), we present the per-component correlation plots for total α and P predictions for the ML-POLY-A (ML-POLY-B) model. All these figures demonstrate that symmetry-adapted Gaussian process regression (SA-GPR) can handle cluster and bulk structures equally well. Since the POLY2VS force-field uses a molecular decomposition of the P , and SA-GPR utilizes an atomic decomposition underneath, it is possible to analyze how well the molecular quantities are being represented. In Fig. 8 and 9, we present the corresponding plots for the molecular predictions. The errors obtained for molecular quantities are much larger than the ones obtained for the total quantities. This fact is not surprising since our models are trained on real observables (i.e. total P and total α) and we are not using any physical constraints on our models beyond the symmetry considerations.

In Fig. 10 and Fig. 11, we present the absolute percentage errors of the molecular predictions for ML-POLY-A and ML-POLY-B models, respectively, as a function of distance from the interface in the same setup used to compute the Vibrational sum frequency generation (VSFG) spectra, i.e. water slab structures. Note that these structures are not included in the training sets. Both models show similar performance, with ML-POLY-B performing slightly better, even though ML-POLY-A was trained on bulk structures exclusively, and surprisingly the predictions are more accurate in the vicinity of the interface. While the

error distributions for the diagonal components of α are relatively narrow around the mean value, the off-diagonal elements show a more uniform distribution with errors up to 100%. We believe that the larger errors in the latter case are due to the smaller relative values of the off-diagonal elements with respect to the diagonal ones. The polarization components show a better performance than the off-diagonal elements but worse than the diagonal elements of α . Note that, as it is shown in the main text (and in Fig. 12 below), all the $\chi^{(2)}$ component are predicted satisfactorily except $\chi_{zxx}^{(2)}$ which utilizes one of the off-diagonal components of α .

ADDITIONAL FIGURES

In Fig. 12, we present calculations for the imaginary part of $\chi^{(2)}$ using GPR and POLY2VS α - P surfaces using trajectories obtained with POLY2VS potential energy surface (PES). In Fig. 13, we compare the predicted spectra using different PES but the same POLY2VS α - P surfaces using different cutoff values (see Eq. 1). In Fig. 14, we compare the density and orientation profiles obtained with *ab initio* and neural-network PES. In Fig. 15 we present the real part of $\chi^{(2)}$ corresponding to the simulations shown in Fig. 3 in the main text. Finally, in Fig. 16 we present imaginary part of $\chi^{(2)}$ obtained using three different methods to propagate the nuclei: classical nuclei molecular dynamics (MD), thermostated ring polymer molecular dynamics (TRPMD)^{12,13} and centroid molecular dynamics (CMD)^{14,15}.

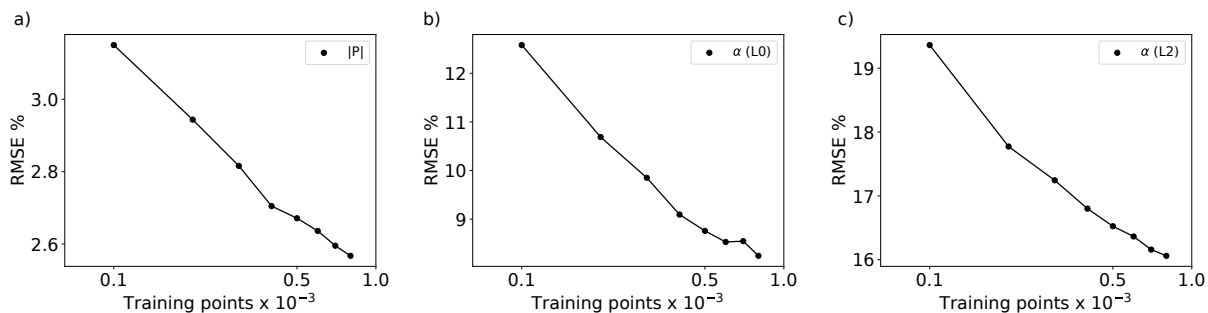


FIG. 1: Learning curve of total polarization (a), $L0$ component of α (b), and $L2$ component of α for ML-POLY-A model

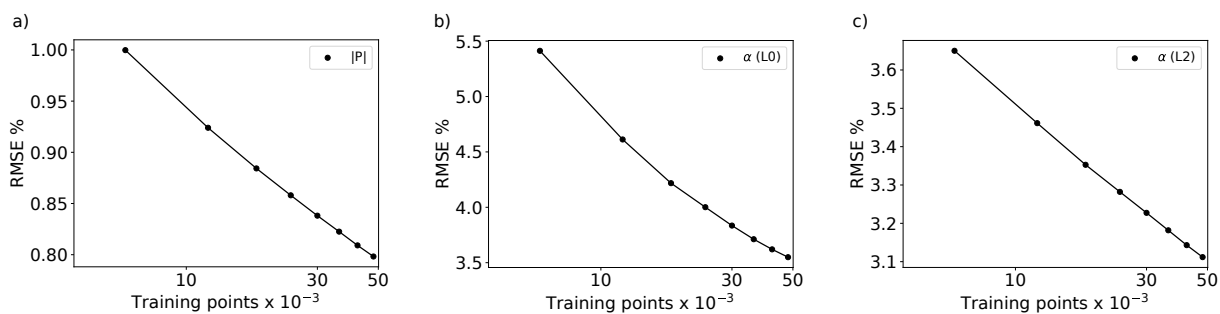


FIG. 2: Same as 1 for ML-POLY-B model

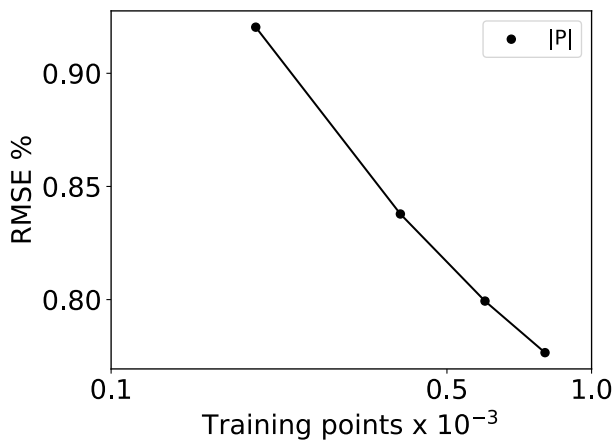


FIG. 3: Learning curve of total polarization for ML-PBE0-A model.

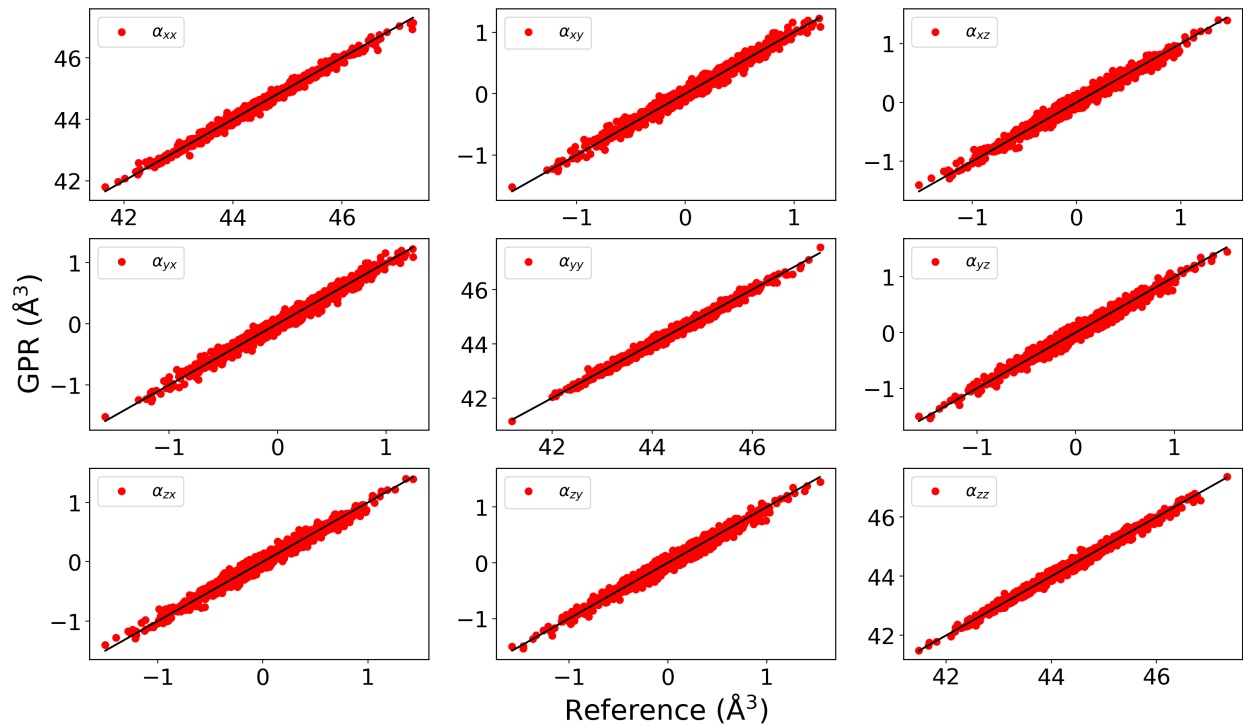


FIG. 4: Prediction of total α components for ML-POLY-A model.

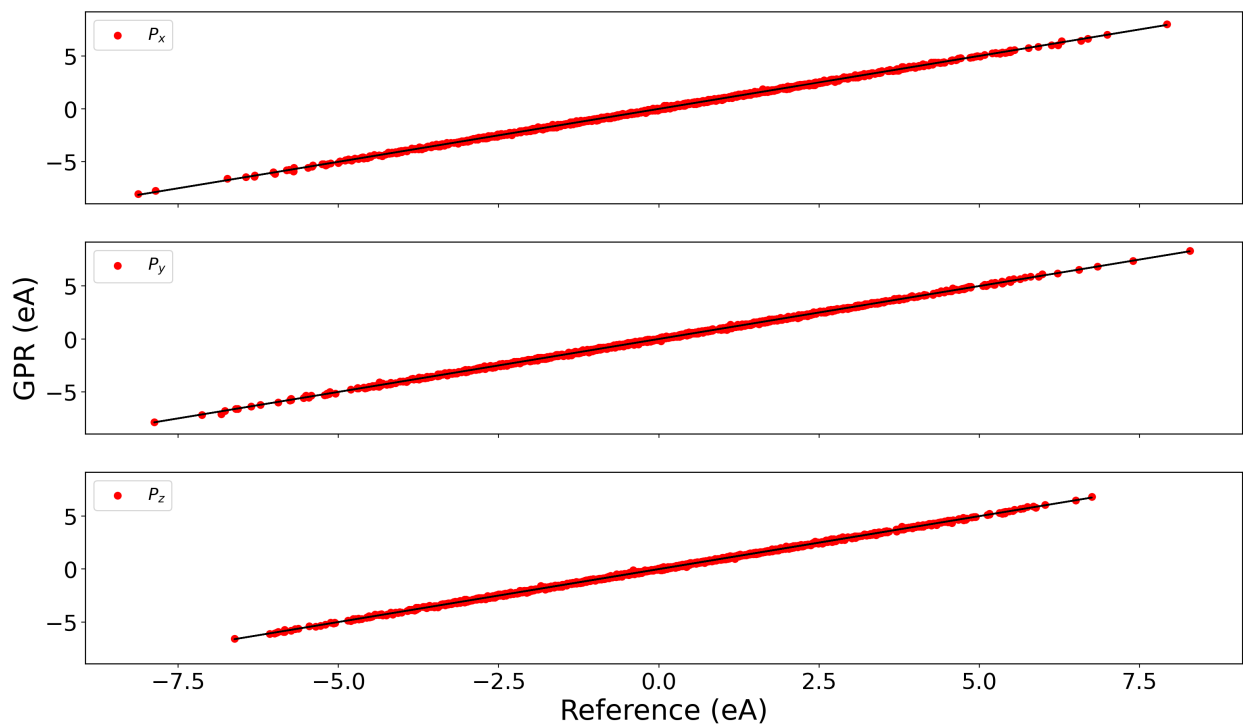


FIG. 5: Prediction of total P for ML-POLY-A model.

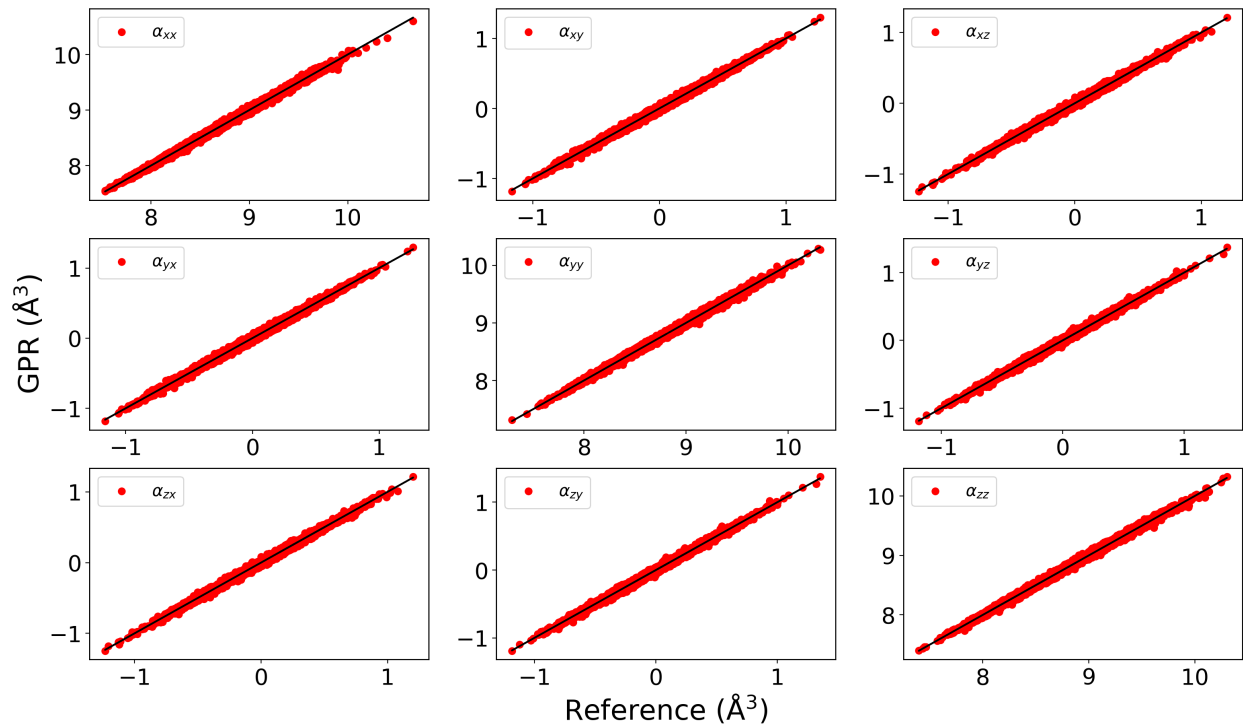


FIG. 6: Prediction of total α components for ML-POLY-A model.

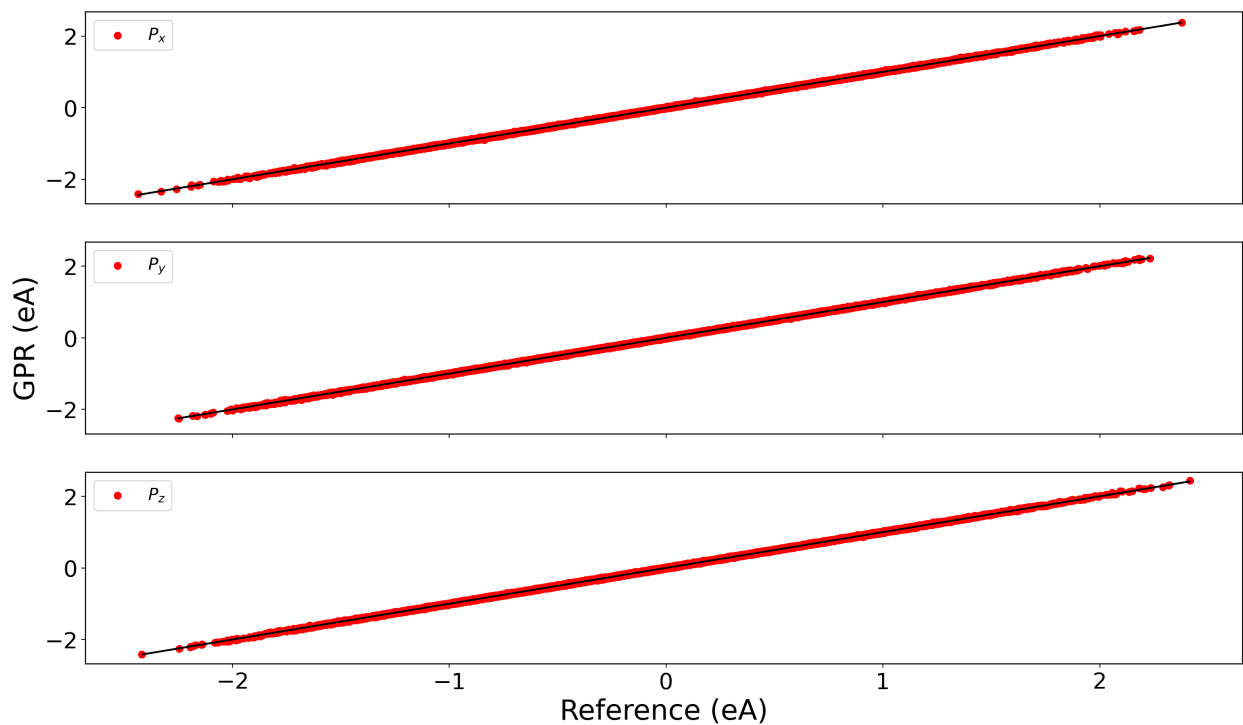


FIG. 7: Prediction of total P for ML-POLY-B model.

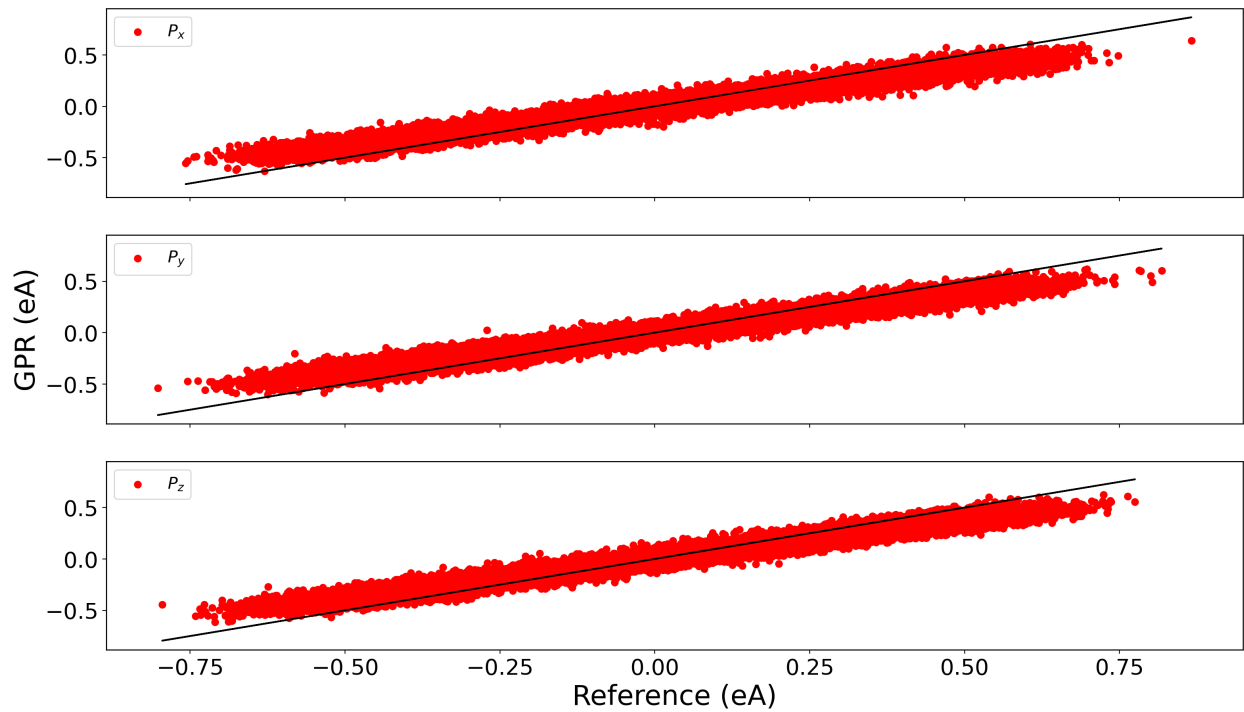


FIG. 8: Prediction of molecular P of ML-POLY-A model.

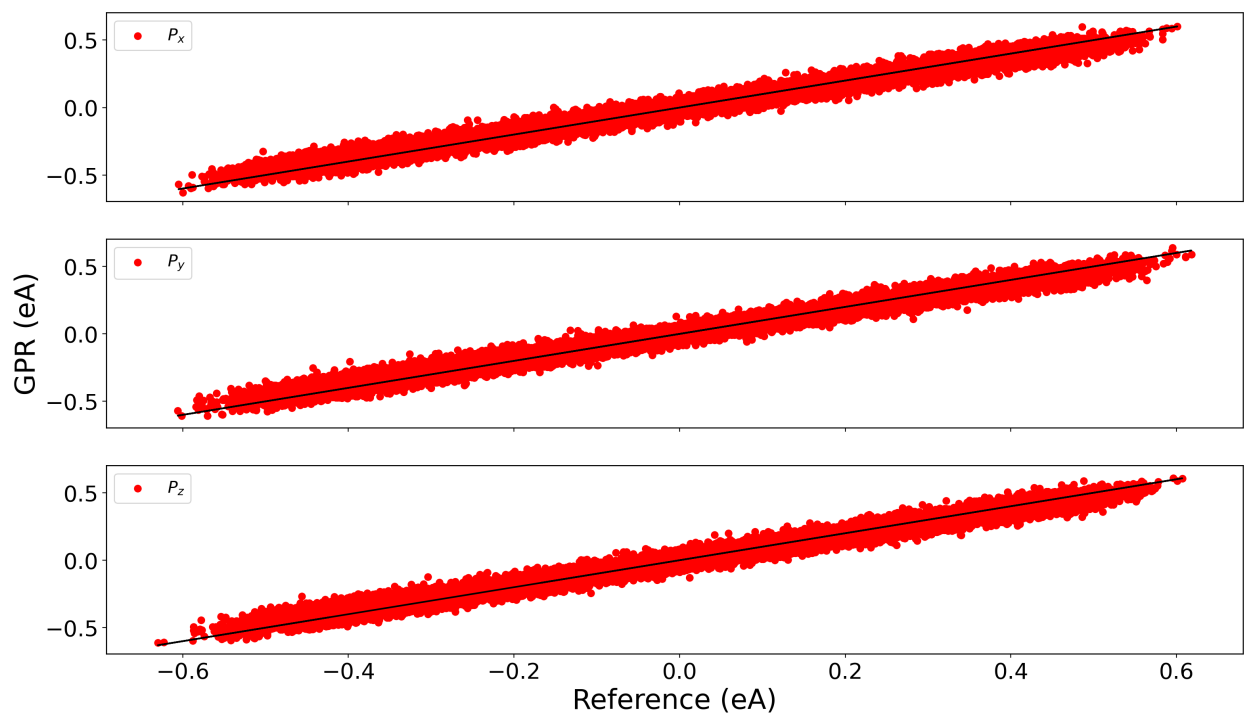


FIG. 9: Prediction of molecular P of ML-POLY-B model on water hexamers

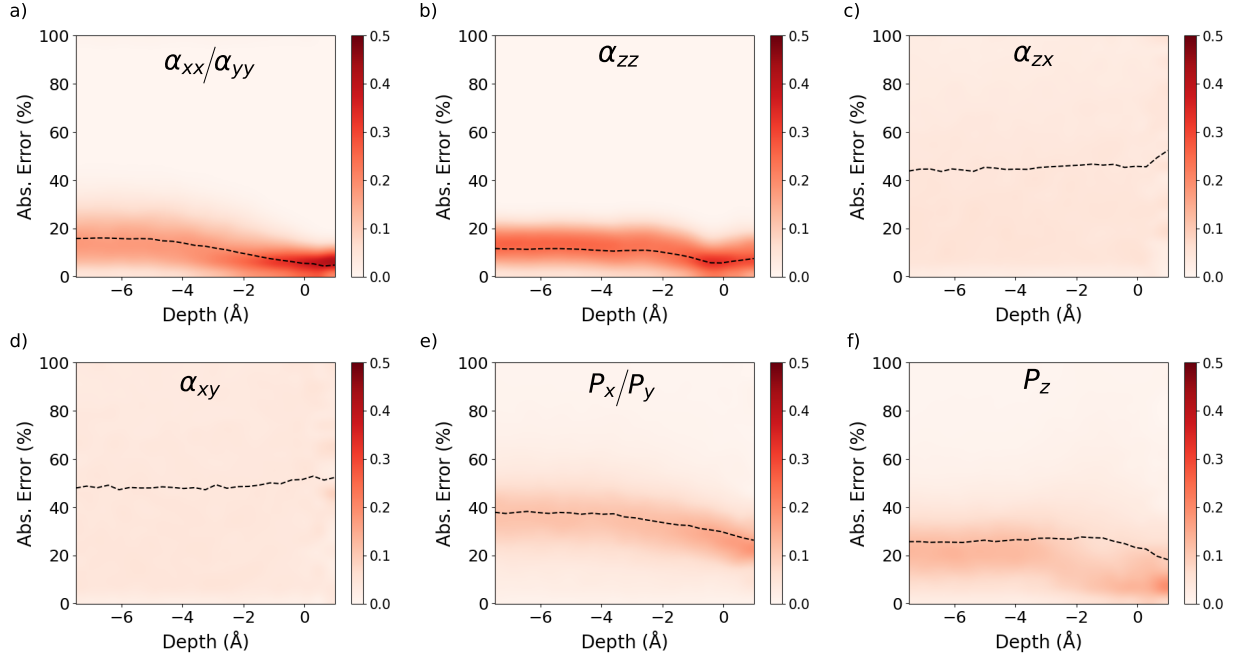


FIG. 10: Absolute error histograms for molecular α and P predictions as a function of distance to the interface using the ML-POLY-A model. Depth distances were computed with respect to the instantaneous interface¹⁶. Black dashed lines correspond to average values.

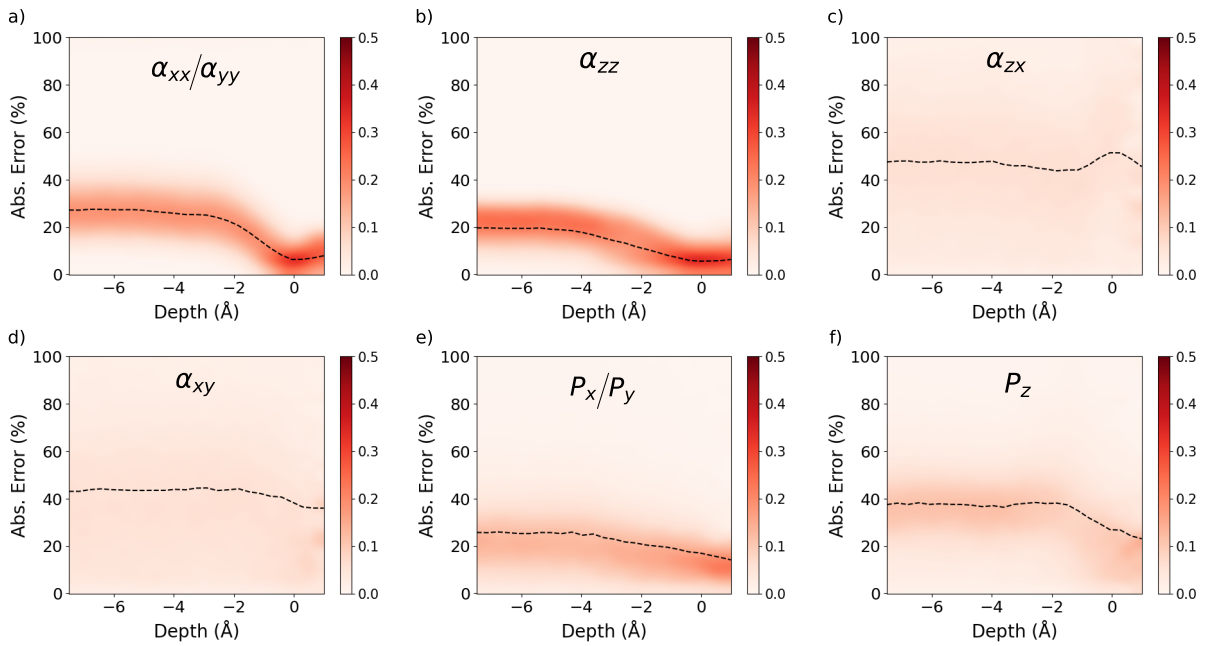


FIG. 11: Same as 10 for ML-POLY-B model.

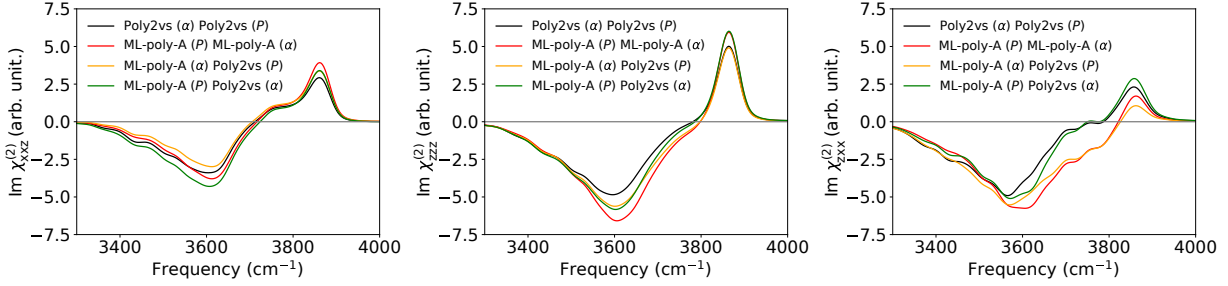


FIG. 12: Imaginary part of non-zero and independent $\chi^{(2)}$ components of the water/air interface using different combinations of POLY2VS and ML-POLY-A P and α surfaces for a slab geometry made of 160 water molecules. This test was performed for a shorter trajectory, thus the increased noise in the signal with respect other figures.

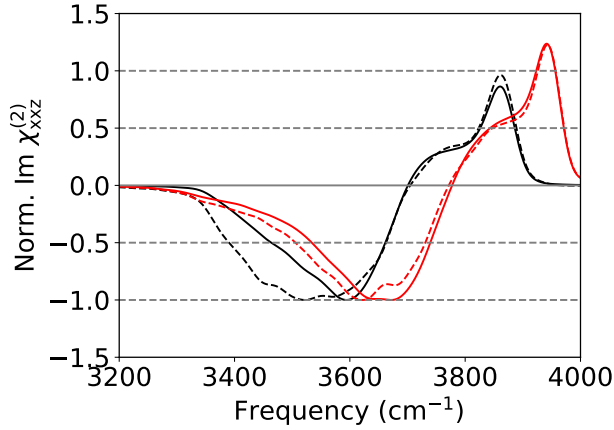


FIG. 13: Imaginary part of $\chi_{xxz}^{(2)}$ of the water/air interface using the POLY2VS P and α surfaces combined with POLY2VS potential energy surface (PES) (black) and HDNNP trained on revPBE0-D3 data PES (red). Solid and dashed lines correspond to calculation 1 Å and 4 Å cutoff values, respectively. Data has been normalized at the H-bonded band to ease comparison.

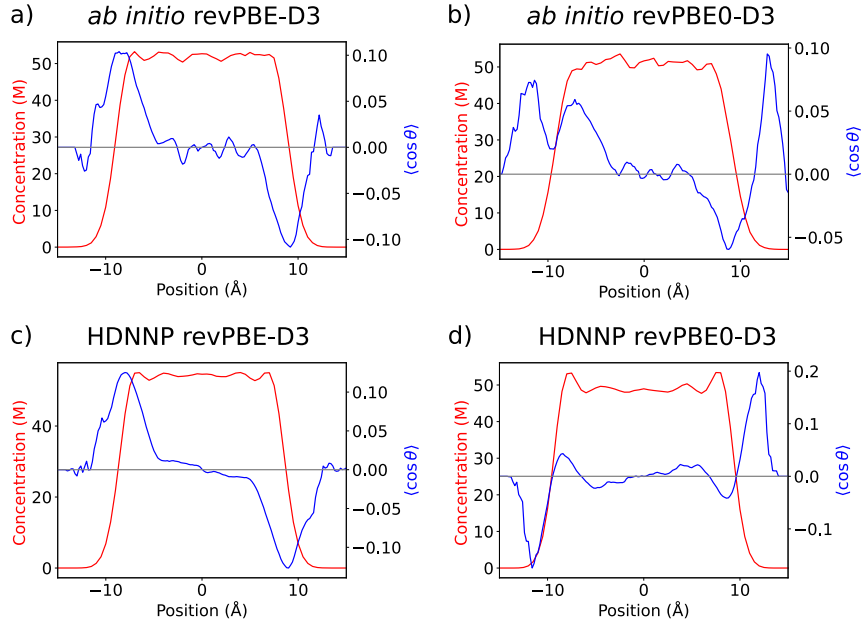


FIG. 14: Water concentration and $\cos(\theta)$ profiles along the direction orthogonal to the slab surface. The center of the slab is set 0 \AA . θ corresponds to the angle between the water bisector and the direction orthogonal to the water/air interface.

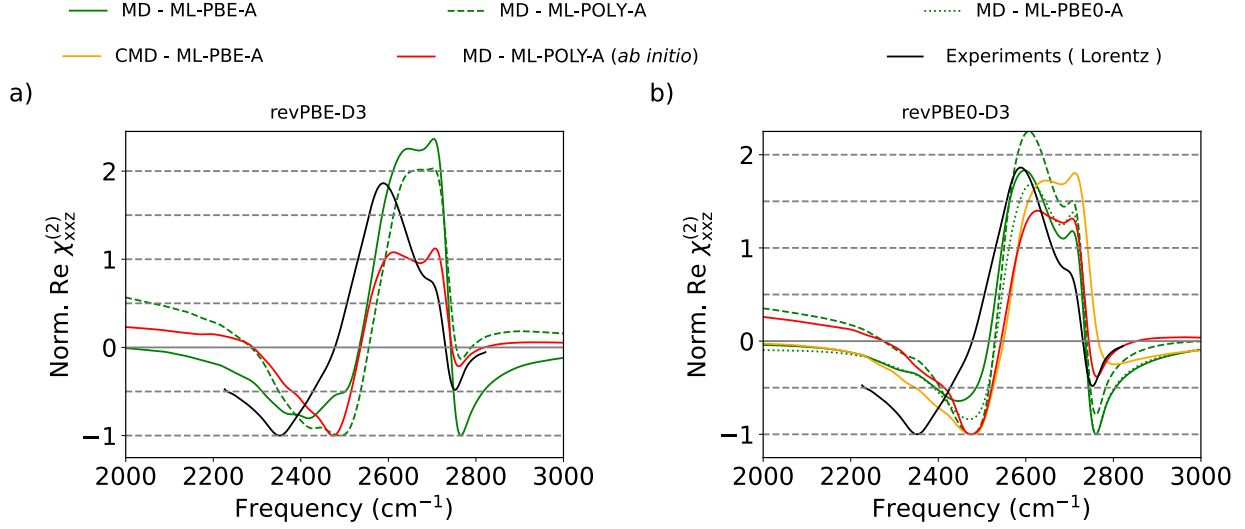


FIG. 15: Normalized Real part of χ_{xxz} spectra of the D_2O /air interface at 300K. Simulated spectra using revPBE-D3 (left) and revPBE0-D3 (right) exchange correlation (XC) functionals. Classical molecular dynamics (MD) simulations using high-dimensional neural networks (HDNNP)s are presented by solid (ML-PBE-A), dashed (ML-POLY-A), and dotted (ML-PBE0-A) green lines. centroid molecular dynamics (CMD) simulations are depicted with solid orange lines while results based on direct *ab initio* trajectories are depicted with red lines. Experimental spectra are depicted with solid black lines and horizontal gray lines have been added to guide the eye. Spectra have been rigidly shifted to match experimental spectra. Experimental spectra are corrected by the appropriate Fresnel factors, assuming the Lorentz model (black dotted lines) for the interfacial dielectric constant¹⁷. To allow a comparative analysis, we present the spectra, normalized such that the minimum intensity has an intensity of minus one.

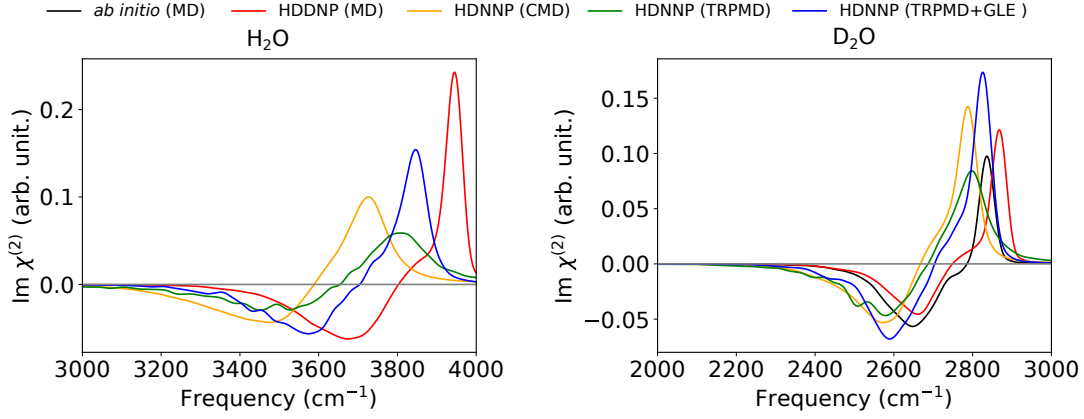


FIG. 16: Imaginary part $\chi^{(2)}$ of the water/air interface calculated using the ssVVCF approximations¹⁸ and different molecular dynamics (MD, red line), centroid molecular dynamics (CMD, orange line), thermostated ring polymer molecular dynamics (TRPMD, orange line), and thermostated ring polymer molecular dynamics tuned with a generalized Langevin thermostat (TRPMD+GLE, blue line). All simulations were performed at 300K employing the HDNNP trained on revPBE0-D3 data.

REFERENCES

- ¹N. K. Kaliannan, A. H. Aristizabal, H. Wiebeler, F. Zysk, T. Ohto, Y. Nagata, and T. D. Kühne, “Impact of intermolecular vibrational coupling effects on the sum-frequency generation spectra of the water/air interface,” *Molecular Physics* **118**, 1620358 (2020).
- ²D. R. Moberg, S. C. Straight, and F. Paesani, “Temperature dependence of the air/water interface revealed by polarization sensitive sum-frequency generation spectroscopy,” *J. Phys. Chem. B* **122**, 4356–4365 (2018).
- ³T. D. Kühne, M. Iannuzzi, M. Del Ben, V. V. Rybkin, P. Seewald, F. Stein, T. Laino, R. Z. Khaliullin, O. Schütt, F. Schiffmann, *et al.*, “Cp2k: An electronic structure and molecular dynamics software package-quickstep: Efficient and accurate electronic structure calculations,” *The Journal of Chemical Physics* **152**, 194103 (2020).
- ⁴J. VandeVondele and J. Hutter, “Gaussian basis sets for accurate calculations on molecular systems in gas and condensed phases,” *The Journal of Chemical Physics* **127**, 114105 (2007).
- ⁵S. Goedecker, M. Teter, and J. Hutter, “Separable dual-space gaussian pseudopotentials,” *Physical Review B* **54**, 1703 (1996).
- ⁶C. Hartwigsen, S. Goedecker, and J. Hutter, “Relativistic separable dual-space gaussian pseudopotentials from h to rn,” *Physical Review B* **58**, 3641 (1998).
- ⁷M. Guidon, J. Hutter, and J. VandeVondele, “Auxiliary density matrix methods for hartree-fock exchange calculations,” *Journal of Chemical Theory and Computation* **6**, 2348–2364 (2010).
- ⁸M. Guidon, J. Hutter, and J. VandeVondele, “Robust periodic hartree foek exchange for large-scale simulations using gaussian basis sets,” *Journal of Chemical Theory and Computation* **5**, 3010–3021 (2009).
- ⁹R. King-Smith and D. Vanderbilt, “Theory of polarization of crystalline solids,” *Physical Review B* **47**, 1651 (1993).
- ¹⁰R. Resta, “Macroscopic polarization in crystalline dielectrics: the geometric phase approach,” *Reviews of modern physics* **66**, 899 (1994).
- ¹¹V. Kapil, D. M. Wilkins, J. Lan, and M. Ceriotti, “Inexpensive Modelling of Quantum Dynamics using Path Integral Generalized Langevin Equation Thermostats,” *J. Chem. Phys.* **152**, 124194 (2020), arXiv:/arxiv.org/abs/1912.03189 [https:].

- ¹²M. Rossi, M. Ceriotti, and D. E. Manolopoulos, “How to remove the spurious resonances from ring polymer molecular dynamics,” *J. Chem. Phys.* **140**, 234116 (2014).
- ¹³M. Rossi, V. Kapil, and M. Ceriotti, “Fine tuning classical and quantum molecular dynamics using a generalized langevin equation,” *J. Chem. Phys.* **148**, 102301 (2018).
- ¹⁴S. Jang and G. A. Voth, “A derivation of centroid molecular dynamics and other approximate time evolution methods for path integral centroid variables,” *J. Chem. Phys.* **111**, 2371–2384 (1999).
- ¹⁵J. Cao and G. A. Voth, “The formulation of quantum statistical mechanics based on the feynman path centroid density. ii. dynamical properties,” *J. Chem. Phys.* **100**, 5106–5117 (1994).
- ¹⁶A. P. Willard and D. Chandler, “Instantaneous liquid interfaces,” *J. Phys. Chem. B* **114**, 1954–1958 (2010).
- ¹⁷X. Yu, K.-Y. Chiang, C.-C. Yu, M. Bonn, and Y. Nagata, “On the fresnel factor correction of sum-frequency generation spectra of interfacial water,” *J. Chem. Phys.* **158**, 044701 (2023).
- ¹⁸T. Ohto, K. Usui, T. Hasegawa, M. Bonn, and Y. Nagata, “Toward ab initio molecular dynamics modeling for sum-frequency generation spectra; an efficient algorithm based on surface-specific velocity-velocity correlation function,” *J. Chem. Phys.* **143**, 124702 (2015).